ELSEVIER

Contents lists available at ScienceDirect

# **Quaternary Science Reviews**

journal homepage: www.elsevier.com/locate/quascirev





# Sedimentary stratigraphy and provenance off Dronning Maud Land (East Antarctica) during the mid-Pleistocene transition: Implications for paleoclimate and ice dynamics

Cheng-Cheng Wang <sup>a,b,\*</sup>, Sidney Hemming <sup>b</sup>, Suzanne O'Connell <sup>c</sup>, Eliza Carter <sup>c</sup>, Troy Rasbury <sup>d</sup>, Trevor Williams <sup>e</sup>, Brendan T. Reilly <sup>b</sup>, Stefanie Brachfeld <sup>f</sup>, Sanzhong Li <sup>a</sup>

- <sup>a</sup> Frontiers Science Center for Deep Ocean Multispheres and Earth System, Key Lab of Submarine Geosciences and Prospecting Techniques, MOE and College of Marine Geosciences, Ocean University of China, Qingdao, 266100, China
- <sup>b</sup> Lamont-Doherty Earth Observatory, Columbia University, Palisades, NY, 10964, USA
- Department of Earth and Environmental Sciences, Wesleyan University, Middletown, CT, 06459, USA
- <sup>d</sup> Department of Geosciences, Stony Brook University, Stony Brook, NY, 11794, USA
- <sup>e</sup> International Ocean Discovery Program, Texas A&M University, College Station, TX, 77845, USA
- f Earth and Environmental Studies, Montclair State University, Montclair, NJ, 07043, USA

#### ARTICLE INFO

Handling editor: Dr C. O'Cofaigh

Keywords:
Strontium isotope stratigraphy
Foraminifera
Ice-rafted debris
Iceberg discharge
40Ar/39Ar thermochronology
Weddell Sea
Antarctic Ice Sheet

#### ABSTRACT

Glacial-marine sediments from the Antarctic continental margin provide a record of depositional environment, oceanographic variability and ice dynamics that is tapped with scientific ocean drilling. This study focuses on Ocean Drilling Program Core 693A-2R, a 9.7 m sediment core retrieved from near the continental margin of the Archean Grunehogna Craton in Dronning Maud Land (DML), East Antarctica. The results contribute to a better understanding of ice-shelf behavior in DML during the mid-Pleistocene transition (MPT), a well-known transition from 40-kyr to 100-kyr cycle periods. The age model, constructed based on Sr isotope stratigraphy and geomagnetic reversals, indicates that the core spans 1.20 to 0.65 Ma. The dynamic behavior of DML ice shelves with periodic iceberg calving is revealed by the glacial-interglacial variation in sedimentation patterns, with interglacials characterized by higher concentrations of ice-rafted debris (IRD) associated with enhanced paleoproductivity than glacial intervals. The responses of DML ice shelves to warm climates are represented by a prolonged interglacial period at 1.0-1.1 Ma (MIS 31-27) and significant interglacial expressions during MIS 19 and 17. The  $^{40}$ Ar/ $^{39}$ Ar ages of individual ice-rafted hornblende grains are compared with the on-land geology of DML and neighboring regions to determine the provenances of IRD. Specifically, 40Ar/39Ar results record primarily late Neoproterozoic to Cambrian ages (600-400 Ma) with a predominant peak of 520-480 Ma. This Pan-African/Ross orogeny signature is very common in East Antarctica but is not found in the most proximal margin of the Grunehogna Craton, and is instead associated with the region of DML several hundred kilometers east of the deposition site. This indicates that significant discharges of icebergs occurred in the remote DML, which were then transported by the westward-flowing Antarctic Coastal Current to deposit IRD at the studied site during the MPT. This study establishes a confirmed MPT sedimentary sequence off DML, against which future MPT proxy records from the Weddell Sea embayment and other sectors in Antarctica can be compared and correlated, and provides a basis for more detailed analyses of the response of DML ice sheet to Pleistocene climate variations.

## 1. Introduction

The East Antarctic Ice Sheet (EAIS) has traditionally been viewed as a stable, slowly evolving component within the climate system, ostensibly

less susceptible to past global climatic fluctuations compared to the marine-based West Antarctic Ice Sheet (WAIS). However, recent geological and modeling investigations have shown that the EAIS, especially the marine-based catchments and outlet glaciers, exhibits a

<sup>\*</sup> Corresponding author. Frontiers Science Center for Deep Ocean Multispheres and Earth System, Key Lab of Submarine Geosciences and Prospecting Techniques, MOE and College of Marine Geosciences, Ocean University of China, Qingdao, 266100, China.

E-mail address: ccwang@ldeo.columbia.edu (C.-C. Wang).

more dynamic evolution that is tightly coupled to the global climate system since the inception of continental-scale ice sheets at ca. 34 Ma (e. g., Gulick et al., 2017; Stokes et al., 2022). The mid-Pleistocene transition (MPT) represents a critical period in climate history, characterized

by a switch in cycle amplitudes and periods from 41-kyr to approximately 100-kyr, concurrent with global sea surface temperature (SST) cooling and increased ice volume (Clark et al., 2006; McClymont et al., 2013; Ford and Raymo, 2020). Despite ongoing debates regarding the

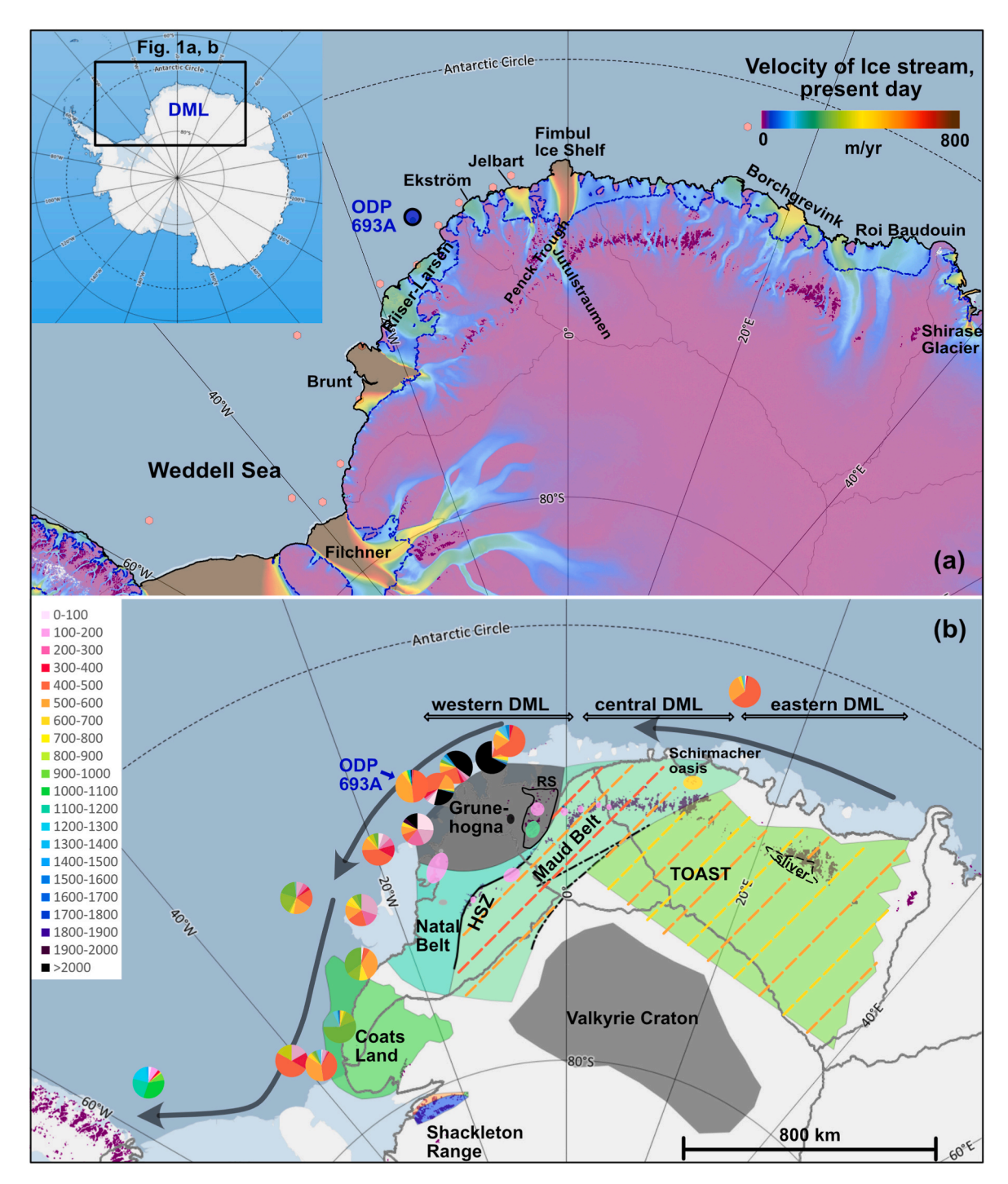


Fig. 1. (a) Distribution and ice velocity of Antarctic ice streams on the continental margin of Dronning Maud Land (DML) (from Rignot et al., 2017) with the inset showing the location of DML in East Antarctica. The black solid line and blue dashed line indicate the coastline and the grounding line respectively. The locations of ODP Hole 693A (70°49.892′S, 14°34.410′W) and the studied core tops in Pierce et al. (2014) (smaller pink symbols) are marked. The map elements were acquired through the Quantarctica 3.2 GIS package (Matsuoka et al., 2021; http://www.quantarctica.org/). (b) Geologic map showing inferred geological domains in DML (domain boundaries from Golynsky et al., 2018), with typical Archean to Mesozoic outcrops indicated by colored shapes. Pie charts show hornblende <sup>40</sup>Ar/<sup>39</sup>Ar ages in this study and published ages along the margin of DML and its adjacent regions (from Pierce et al., 2014, corresponding to the plotted locations in Fig. 1a). The same color legend, on the left side of the diagram, is used for showing geology domains and pie charts. The dark grey arrows represent the Antarctic Coastal Current. The region to the east of the HSZ has been widely overprinted by Pan-African metamorphism (marked with yellow and orange dash lines). See sections 2.2 and 5.2 for detailed descriptions on geology compositions and age correlations. Abbreviations: TOAST, Tonian Oceanic Arc Super Terrane; HSZ, Heimefront Shear Zone; RS, Ritscherflya Supergroup.

impact of the dynamic evolution of the Antarctic Ice Sheet (AIS) on varying paleoclimate conditions during the MPT (e.g., Raymo et al., 2006; Elderfield et al., 2012), there is evidence showing that the Southern Ocean and the AIS responded to this climate transition with a northward migration of the Polar Front and a significant ice-sheet expansion during MIS 24–22, 940–865 ka (Pollard and DeConto, 2009; Kemp et al., 2010; Elderfield et al., 2012; Sutter et al., 2019).

Sediments deposited at the Antarctic continental margin possess significant potential for recording ice dynamic response to climate forcings regarding grounding line adjustments, ice shelf instability, and repeated advances and retreats of ice sheets. The multifaceted evidence provided by sedimentary records, such as the abundance and provenances of ice-derived debris (IRD) and clay minerals, concentrations of biogenic material and elements, and C and O isotopes of calciferous fossils, have been used as climatic proxies to infer the variations in sedimentary environments and ice sheet dynamics during the Pleistocene (e.g., Wilson et al., 2018; Holder et al., 2020; Hillenbrand et al., 2021; Wu et al., 2021). These have revealed a pronounced glacial-interglacial rhythm in sedimentation and productivity within the continental margin sediments of various sectors of East Antarctica, which, frequently but not always, correlate well with the LR04 benthic δ<sup>18</sup>O stack (Wilson et al., 2018; Holder et al., 2020). However, individual catchments and ice streams of the AIS may exhibit different sensitivities to climate and ocean forcings and diverse dynamic behavior (Livingstone et al., 2012; Golledge et al., 2017; Mas e Braga et al., 2023), and the response of the EAIS to major climate changes, particularly in the context of warmer climates, can be non-uniform (Teitler et al., 2015; Holder et al., 2020). This highlights the importance of correlating and comparing sedimentary proxy records across different Antarctic sectors to construct a more comprehensive understanding of the dynamic responses of the AIS to key climate periods.

Compared to other sectors of Antarctica, the Weddell Sea embayment and the ocean off Dronning Maud Land (DML) have been less frequently visited by scientific ocean drilling expeditions, probably due to a consistently robust sea ice cover persisting even through the austral summer. Ice shelves across DML, from the Riiser-Larsen to the Roi Baudouin ice shelf (Fig. 1a), constitute approximately 25% of the total ice shelf area in East Antarctica, with an ice front flux representing 13% of East Antarctica's iceberg calving (Rignot et al., 2013). Recent studies have revealed the sensitivity of the ice sheet in DML to late Quaternary climate variations, marked by an ice thickening during the Last Glacial Maximum (LGM, ca. 21 ka) and substantial thinning of tens to over one hundred meters during the Holocene (Andersen et al., 2020; Suganuma et al., 2022). However, a significant knowledge gap exists in our understanding of DML ice dynamics during the MPT and the impacts on glacial-marine sedimentation offshore DML.

To place the inferred glacial-environmental events into a global context requires a robust chronological framework. However, establishing a reliable chronological framework for sedimentary records on the continental margin of Antarctica is notoriously challenging. The continental margins, particularly the continental shelf and slope, are zones of dynamic interaction between ocean currents, gravity currents, ice shelves, and grounded ice, resulting in non-steady-state deposition. Processes such as ice sheet advance and retreat can cause erosion and hiatuses, for example, erosional unconformities are present in the Miocene-Pliocene sedimentary sequences off DML (Huang and Jokat, 2016). In addition, the prevalent methodology for obtaining absolute ages, which relies on radioisotope dating of calcareous fossils, has a significant limitation in the context of Pleistocene sediments from the Southern Ocean, where such fossils are notably scarce. The Pleistocene sedimentation off DML has an average sediment accumulation rate of 1-2 cm/kyr (Barker and Kennett, 1988; Grobe and Mackensen, 1992), and such low sedimentation rates intensify the challenges of constructing a high-resolution age-depth model.

This study focuses on Ocean Drilling Program (ODP) Core 693A-2R, which contains ice-rafted debris (IRD) and planktonic foraminifera and

thus allows for a multi-proxy study of stratigraphy, provenance and sedimentation patterns to constrain DML ice dynamics during the MPT. This study 1) develops an age model using a combination of Sr isotope stratigraphy and paleomagnetic measurements; 2) determines the provenances of IRD by performing <sup>40</sup>Ar/<sup>39</sup>Ar analyses on individual hornblende grains; 3) describes sedimentation characteristics with glacial-interglacial changes in IRD supply and productivity; and 4) contributes to a better understanding of the dynamic responses of DML ice shelves to climate variations during the MPT.

#### 2. Site description and regional geology

#### 2.1. ODP Hole 693A: location and sedimentation

ODP Site 693, one of the three sites drilled during ODP Leg 113 on the DML continental margin in East Antarctica (Sites 691, 692, and 693), is located on a mid-slope bench at a water depth of 2359 m (Fig. 1a). The drilling attempts at nearby Sites 691 and 692 were mostly unsuccessful with very poor recovery, with Quaternary sedimentary sequence only preserved in the uppermost 1–2 m below sea floor (mbsf) (Barker and Kennett, 1988). In contrast to Hole 693B, which was washed to a depth of 233.8 mbsf and thus failed to recover the Quaternary records, Hole 693A successfully recovered 51 cores, achieving a depth of 483.9 mbsf and culminating in Lower Cretaceous claystones (Barker and Kennett, 1988). As such, Hole 693A provides a rare opportunity for studying Pleistocene sedimentation off DML.

The sediments recovered at ODP Hole 693A are primarily terrigenous with minor biogenic calcareous (i.e., foraminifers) and siliceous (diatoms, sponge spicules, and radiolarians) content (Barker and Kennett, 1988). Pleistocene sediments are preserved in the uppermost three cores, exhibiting a significantly lower accumulation rate (~1 cm/kyr) in comparison to the Pliocene and late Miocene periods (2-5 cm/kyr). Barker and Kennett (1988) suggested that the decreased terrigenous flux could be attributed to the intensification of Antarctic glaciation and the permanent grounding of the ice shelf to the continental shelf edge during the Pleistocene. The sediment at the top of the drilling in Core 1 exhibits soupy to soft mud, which has been extensively disturbed and homogenized by drilling (Barker and Kennett, 1988). Here we focus on Core 2, which recovered a 9.7 m sequence in 7 sections (2.5-12.2 mbsf) and consisted mainly of foraminifera bearing sandy silt, clayey to silty mud with IRD and dropstones. The age estimations presented in the preliminary report were primarily derived from biostratigraphy and magnetostratigraphy constructed from natural remanent magnetization (NRM) measurements. The Brunhes-Matuyama boundary (ca. 800-770 ka) was identified at 8 mbsf (Grobe et al., 1990), but the digital NRM data and any data collected after alternating field (AF) demagnetization are not available.

#### 2.2. Geology of Dronning Maud Land and adjacent regions

East Antarctica preserves geological evidence of its past connections with India, Australia, and Africa in the configuration of Gondwana, and the DML region represents the part of the geology associated with southern Africa in Gondwana (e.g., Ebbing et al., 2021). DML represents an assemblage of multiple Archean to Neoproterozoic geological domains that were finally assembled during the formation of the East African-Antarctic Orogen (EAAO, Fig. 1b, Jacobs et al., 1998). ODP Hole 693A is located off the Archean Grunehogna Craton, which has a geological affinity to the Proto-Kalahari Craton in southern Africa (Marschall et al., 2010). The Archean basement of the Grunehogna Craton was dated at ca. 3.5-3.0 Ga (Marschall et al., 2010), and ca. 2.8 Ga granite has been recently discovered to the east of the very eastern margin of the craton (Grantham et al., 2023). It is worth mentioning that on the eastern margin of the Grunehogna Craton, the Ritscherflya Supergroup represents a Mesoproterozoic sedimentary sequence that was deposited during 1130-1110 Ma (Fig. 1b, Marschall et al., 2013), and subsequently it was intruded by massive mafic sills at ca. 1110–1100 Ma (Hanson et al., 2006). The detrital zircons from the Ritscherflya Supergroup show multiple peaks, including dominant peaks of ca. 1130 Ma and ca. 2700 Ma, which were derived from the Grenville-age Maud Belt to the east and the local Archean basement respectively, and subordinate peaks of 1370, 1720–1880 and 2050 Ma (Marschall et al., 2013), but the basement of these ages has not been reported in DML so far.

The Grunehogna Craton is enveloped by the Mesoproterozoic (Grenville-age) orogenic crust to the east and south. The Maud Belt, separated from the Grunehogna Craton to the west by the major Jutulstraumen-Penckgraben rift (Fig. 1a), occupies a significant part of DML, the magmatism of which mainly occurred at 1170-1050 Ma (Wang et al., 2020a). Separated by the Heimefront Shear Zone, the crust to the southwest of the Maud Belt is considered to be connected to the Natal Belt in South Africa, which witnessed slightly older magmatism at 1250-1050 Ma (Wang et al., 2020a). The Coats Land Block (Bertrab-Littlewood-Moltke Nunataks) has very limited geological exposure, and the accessible granite outcrops were dated at ca. 1100 Ma (Loewy et al., 2011). To the south of Coats Land, the geology of the Shackleton Range has been separated into northern, southern, and eastern terranes (Will et al., 2010). The main episode of magmatism in the southern terrane was dated in the interval 1850–1810 Ma, overprinted by a major tectono-metamorphic event at 1710-1680 Ma, while the northern terrane recorded high-grade metamorphism and granitic magmatism at 600-500 Ma. The Eastern Terrane is composed of Grenville-age granitoids dated at ca. 1060 Ma with a ca. 600 Ma metamorphic overprint (Will et al., 2010).

The crust to the east of the Maud Belt is characterized by 1000-900 Ma rocks with a juvenile isotopic composition, and it is referred to as the TOAST (Tonian Oceanic Arc Super Terrane) by Jacobs et al. (2015). Recent geophysical investigations have revealed that the crust located to the south of the TOAST is likely to be an ancient craton (Valkyrie Craton, Golynsky et al., 2018), but the age and boundary of the craton remain undetermined. A significant part of DML has been subjected to protracted Pan-African tectono-thermal overprinting with multiple episodes of metamorphism and magmatism during the formation and evolution of the EAAO. The western front of the EAAO is represented by the Heimefront Shear Zone (Fig. 1b, Jacobs and Thomas, 2004), and the eastern margin of the Grunehogna Craton has also been affected by pan-African events to some extent (Marschall et al., 2013). Specifically, central DML underwent high-grade metamorphism during 580-530 Ma with the peak metamorphism occurring at 570-550 Ma, followed by extensive volumes of late-tectonic granitoid magmatism at 530-480 Ma (Wang et al., 2020b). In eastern DML, metamorphic events mainly occurred at 650-600 Ma and 580-550 Ma accompanied by multiple pulses of granitic magmatism during 650-500 Ma (Elburg et al., 2016). During the break-up of Gondwana, western DML including the Grunehogna Craton witnessed multiple periods of mafic intrusions during ca. 207-175 Ma (Riley et al., 2005), which are considered as an extension of the Karoo large igneous province of southern Africa.

The <sup>40</sup>Ar-<sup>39</sup>Ar ages published from various outcrops across DML primarily fall within a range of approximately 590–450 Ma (most are less than 550 Ma), with only a few older ages of 1100–800 Ma obtained to the west of the western orogenic front of the EAAO (Ruppel et al., 2021). To our knowledge, no <sup>40</sup>Ar-<sup>39</sup>Ar age has been reported in the Grunehogna Craton so far. Nevertheless, the offshore sediments on the continental shelf of the craton suggest a significant decrease in Pan-African age proportions and an increase in Archean and Mesozoic ages compared to those sediments deposited to the east (Fig. 1b, Pierce et al., 2014). This supports the geological interpretation that a substantial portion of the Grunehogna Craton, including the Archean outcrops, has remained unaltered by thermal overprinting since the Archean.

#### 3. Methods

#### 3.1. Sediment processing and sieving

Bulk samples ( $\sim$ 10 cm $^3$ ) were dried, weighed, disaggregated, and wet-sieved through 63 µm sieves with deionized water. The dried coarse fractions (>63 µm) were then sieved through 500-µm and 150-µm sieves to obtain fractions of >500 µm, 150–500 µm and 63–150 µm. For each sample the weight of the >150 µm size fractions was weighted and the weight was divided by the entire weight of the sample to obtain the weight percentage of the >150 µm fraction (Fig. 5c). Density separation with heavy liquids was not performed considering they may cause damage and alteration to foraminifera, thus the >150 µm fraction here includes both terrigenous sediments that are taken as IRD and also biognetic carbonate of foraminifera. Although foraminifera are relatively abundant, they make up a small volumetric percent of the total coarse fractions.

#### 3.2. Strontium isotope analysis

Strontium isotopic measurements were performed at the Facility for Isotope Research and Student Training (FIRST) laboratory at SUNY Stony Brook University. For each sample at a specific depth, 30-50 foraminifera grains (planktonic species N. pachyderma) were handpicked from the 150-500 µm fraction and then cleaned following the procedures of Barker et al. (2003). Following cleaning, samples were dissolved in 1 N HNO3, and Sr was isolated by using Sr-spec© ion exchange resin. Purified Sr was loaded onto degassed rhenium filaments after loading 1 µL of dilute tantalum chloride, and then the filament was heated on the sample loader until it dried slowly. The Sr isotopic ratios were measured on an IsotopX Phoenix 62 thermal ionization mass spectrometer (TIMS), with a 3-sequence dynamic routine measurement of masses 84, 85, 86, 87, and 88 over 192 cycles for each sample, where mass-87 was measured in the Axial, H1, and H2 cups, and masses-84, 85, 86, and 88 were measured in sequentially adjacent cups. Filaments were slowly ramped up to 2.8-3.4 A, with a temperature between 1350 and 1450 °C, to achieve a stable beam intensity on Sr-88. Sr isotopes were corrected for mass fractionation using an <sup>86</sup>Sr/<sup>88</sup>Sr ratio of 0.1194. The analyses were performed with the aliquots of the same sample loaded on at least three different filaments and measured on multiple turrets to avoid any hardware-specific offsets. The long-term 2σ reproducibility of standard NBS SRM 987 was estimated with repeated measurements conducted from August to November 2022. The mean value of NBS 987 over this period (with  $2\sigma$  outliers removed) is  $^{87}\text{Sr}/^{86}\text{Sr}=0.710242\pm$ 0.000007 ( $2\sigma$ , n=39). Thus, all the measurements were normalized to the referenced NBS 987 value of 0.710248 (McArthur et al., 2020) by adding 0.000006. In addition, several in-house Holocene coral standards were included as unknowns to monitor accuracy, and they give a mean  $^{87}$ Sr/ $^{86}$ Sr value of 0.709166  $\pm$  0.000006 (2 $\sigma$ , n = 13). Strontium isotope numerical ages were derived using the LOWESS Sr marine calibration curve updated in McArthur et al. (2020).

## 3.3. Paleomagnetic measurements

The samples for paleomagnetic measurements were collected between 2.5 and 11.5 mbsf with a sampling interval of 10–30 cm. Samples were collected from flat core surfaces, as much as possible, to avoid cracks and curved edges of the core. Unfortunately, the final core section 2R-7 spanning 11.5–12.2 mbsf proved too hard and dry for successful sampling. Samples were taken by pushing a plastic cube with a 2 cm external edge into the working-half sections. NRM measurement and stepwise AF demagnetization were conducted using an AGICO JR6 spinner magnetometer and D-tech AF Demagnetization unit at Montclair State University. Following the NRM measurement, all samples were subject to 3-axis AF demagnetization in peak fields of 10, 20, and 30 mT to remove the drilling overprint, determined by evaluating the

measurements on a vector endpoint diagram. Samples that define a magnetic polarity transition and a subset of the remaining cubes were subjected to further demagnetization up to 60 mT in 10 mT steps (Supplementary File 3). Since the core was collected by rotary drilling, samples within the core are not horizontally oriented, and only the inclination is used for polarity determinations.

# 3.4. Hornblende <sup>40</sup>Ar/<sup>39</sup>Ar dating

Hornblende grains were hand-picked from the 150-500 µm fraction and co-irradiated with the Fish Canyon sanidine monitor standard at the U.S. Geological Survey (USGS) TRIGA reactor in Denver, CO. <sup>40</sup>Ar/<sup>39</sup>Ar ages were measured on a VG5400 noble gas mass spectrometer using single-step CO2 laser fusion at the Lamont-Doherty Earth Observatory (LDEO) argon geochronology lab (AGES: Argon Geochronology for the Earth Sciences). Each hornblende grain was loaded into a pit of a 69-pit disk, and then the disk was loaded into the sample chamber to be baked for 8 h at around 100 °C under a vacuum system to remove atmospheric contamination. Each disk was measured starting with 8-9 blanks to get a stable signal with a low background interference, and analyses of every 8 unknowns were bracketed by analyzing two blanks and an air pipette with an additional blank measurement after the fourth unknown. Data reduction was performed using the MassSpec software package (MassSpec, v.8.248, A. Deino, Berkeley Geochronology Center, USA). The obtained isotopic results were corrected for backgrounds and mass discrimination using measured blanks and air pipettes, assuming the  $^{40}$ Ar/ $^{36}$ Ar ratio of atmosphere is 298.56 (Lee et al., 2006). J values used to calculate ages were based on the co-irradiated Fish Canyon sanidine standard (28.201  $\pm$  0.046 Kuiper et al., 2008), with decay constants from Min et al. (2000).

# 3.5. X-ray fluorescence (XRF) scanning, X-ray and computed tomography (CT) imaging

XRF scanning was conducted on the archive halves using a third-generation Avaatech core scanner (XRF2) at the IODP Gulf Coast Repository at Texas A&M University. Each section was prepared by scraping the core surface using a glass microscope slide to remove the upper  $\sim\!2$  mm of sediment. Three successive scans at 10, 30 and 50 kV were performed on each core section. Raw X-ray spectra were processed using bAxil software (Brightspec), which uses a nonlinear least squares method. The X-ray imaging was also performed at Texas A&M University on a new instrument in development that is now deployed aboard the JOIDES Resolution. Sub-mm IRD grains can be identified in the images. The 3D CT volumes were used to develop an IRD index by identifying the mid-depth of connected voxels with diameter >1 mm with CT#s > 2500 Hounsfield Units (HU), following the methods in Reilly et al. (2019). Identified IRD clasts were binned in 1 cm intervals based on their central depth (Table 3 in Supplementary File 5).

# **Table 1**Sr isotopic compositions and the corresponding ages for each sample.

Sample	MBSF	N	Mean <sup>87</sup> Sr/ <sup>86</sup> Sr	2SE	Mean SIS age (Ma)	Max SIS age (Ma)	Min SIS age (Ma)	Older error (Ma)	Younger error (Ma)
2R-1, 8-9	2.58	3	0.709153	0.000007	0.66	0.83	0.47	0.17	0.19
2R-4, 34-35	7.34	2	0.709145	0.000005	0.85	0.95	0.76	0.10	0.09
2R-4, 93-94	7.93	3	0.709138	0.000006	0.99	1.08	0.87	0.09	0.12
2R-6, 23-24	10.23	4	0.709137	0.000006	1.01	1.11	0.87	0.10	0.14
2R-6, 29-30	10.29	4	0.709136	0.000005	1.02	1.11	0.93	0.09	0.09
2R-6, 44-45	10.44	3	0.709138	0.000007	0.99	1.11	0.85	0.12	0.14
2R-6, 50-51	10.5	4	0.709133	0.000007	1.08	1.17	0.95	0.09	0.13
2R-6, 74-75	10.74	3	0.709124	0.000004	1.21	1.26	1.16	0.05	0.05
2R-7, 22-23	11.72	4	0.709125	0.000005	1.20	1.26	1.12	0.06	0.08
2R-7, 47-48	11.97	1	0.709123	0.000011	1.22	1.37	1.06	0.15	0.16

MBSF, meters below sea floor; N, Number of filaments used for mean calculation. SIS, Strontium isotope stratigraphy; SD, Standard deviation.  $2 \text{ SE} = \sqrt{((2 \text{ SDStandard/sqrt(N)})^2 + (2 \text{ SDSample/sqrt(N)})^2)}$ 

#### 4. Results

#### 4.1. Sr isotope stratigraphy

The mean values of multiple measurements of each sample, and the corresponding age estimates are presented in Table 1. The samples were selected to span the proposed boundary of the Brunhes-Matuyama reversal at a depth of 8 mbsf and to constrain the top and bottom ages of the core, which include one sample at 2.58 mbsf, two samples at 7-8 mbsf, six samples between 10 and 11 mbsf and two samples near 12 mbsf. Five of the 38 measurements have abnormally high or low isotopic ratios and have been excluded from the age model (Supplementary File 2). For example, one measurement from the sample at 7.34 mbsf shows a noticeable deviation from the other two measurements and is interpreted as an outlier. Furthermore, as Sr isotope evolution from the Pleistocene to the present is known to exhibit a monotonic upward trend (McArthur et al., 2020), the <sup>87</sup>Sr/<sup>86</sup>Sr isotopic results are expected to increase as depth decreases. Therefore, the sample at 10.17 mbsf, which shows an isotopic ratio inconsistent with this evolutionary trend, has been excluded from further calculation and discussion.

The mean isotopic ratios for each sample against the respective collection depths and the corresponding ages are plotted in Fig. 2. The sample at the top of the core exhibits an  $^{87}\mathrm{Sr}/^{86}\mathrm{Sr}$  value of  $0.709153\pm0.000007~(2\sigma)$ , yielding a derived age of 0.66~(+0.17,-0.19,n=3) Ma, while the two samples at the very bottom of the core have mean  $^{87}\mathrm{Sr}/^{86}\mathrm{Sr}$  values of  $0.709125\pm0.000005$  and  $0.709123\pm0.000011$ , with derived ages of 1.20~(+0.06,-0.08,n=4) and 1.22~(+0.15,-0.16,n=1) Ma respectively. The two samples obtained at depths between 7 and 8 mbsf exhibit  $^{87}\mathrm{Sr}/^{86}\mathrm{Sr}$  values of  $0.709145\pm0.000005$  and  $0.709138\pm0.000006$  and the derived ages are 0.85~(+0.10,-0.09,n=2) and  $0.99~\mathrm{Ma}~(+0.09,-0.12,n=3)$  respectively. The five remaining samples at 10-11 mbsf mostly have  $^{87}\mathrm{Sr}/^{86}\mathrm{Sr}$  values ranging from 0.709133 to 0.709138 with derived ages ranging from  $0.99~\mathrm{to}~1.08~\mathrm{Ma}$ , while the sample at  $10.74~\mathrm{mbsf}$  has a mean  $^{87}\mathrm{Sr}/^{86}\mathrm{Sr}$  value of 0.709124, which is similar to the two samples at the very bottom of the core.

#### 4.2. Paleomagnetic measurements

After demagnetization at 10–20 mT, the drilling overprint is generally removed for most samples, exposing a characteristic component that trended toward the origin on orthogonal projection diagrams. As illustrated in Supplementary Fig. 1, the AF demagnetization plots of NRM for normal and reverse polarity samples show a highly linear trend towards the origin, with an upward inclination indicating normal polarity and a downward inclination indicating reversed polarity. The directions of the NRM components were determined using Principal Component Analysis (PCA; Kirschvink, 1980) by the paleomagnetic software package Remasoft 3.0, with line-fits anchored to the origin of the diagram. The data points with a maximum angular deviation (MAD) > 5° were discarded (Supplementary File 3). The analyses show that

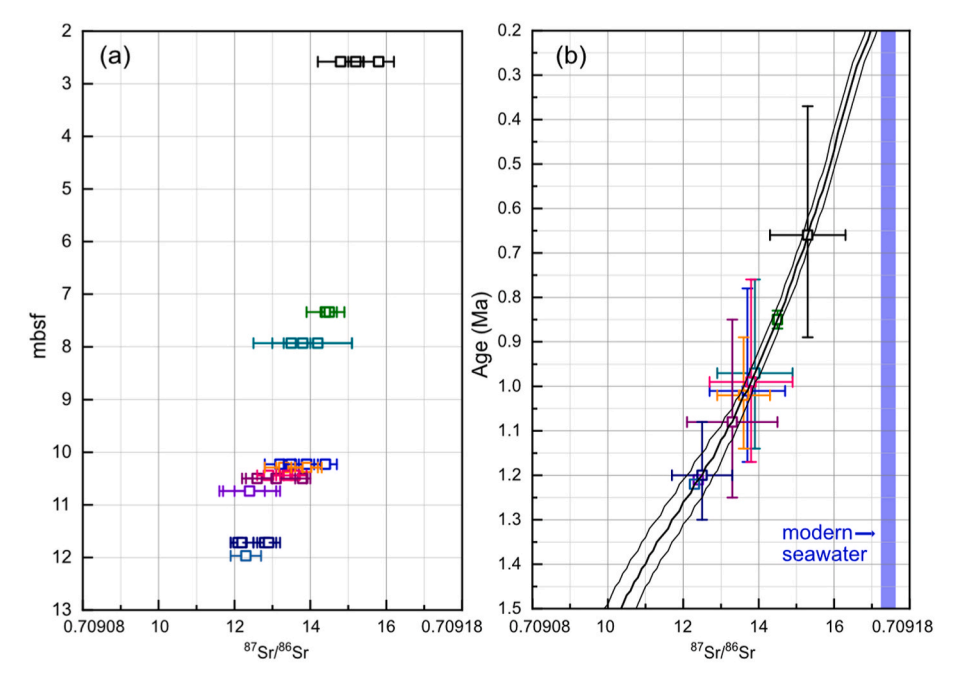


**Fig. 2.** Sr isotopic compositions and corresponding ages. (a) Depth (mbsf) vs. measured <sup>87</sup>Sr/<sup>86</sup>Sr values of foraminifera samples. The results of multiple measurements for each sample are shown with errors (2SE). (b) Sr isotope stratigraphy ages vs. mean <sup>87</sup>Sr/<sup>86</sup>Sr ratios for each sample (Sr isotope curves and values of modern seawater are from McArthur et al., 2020).

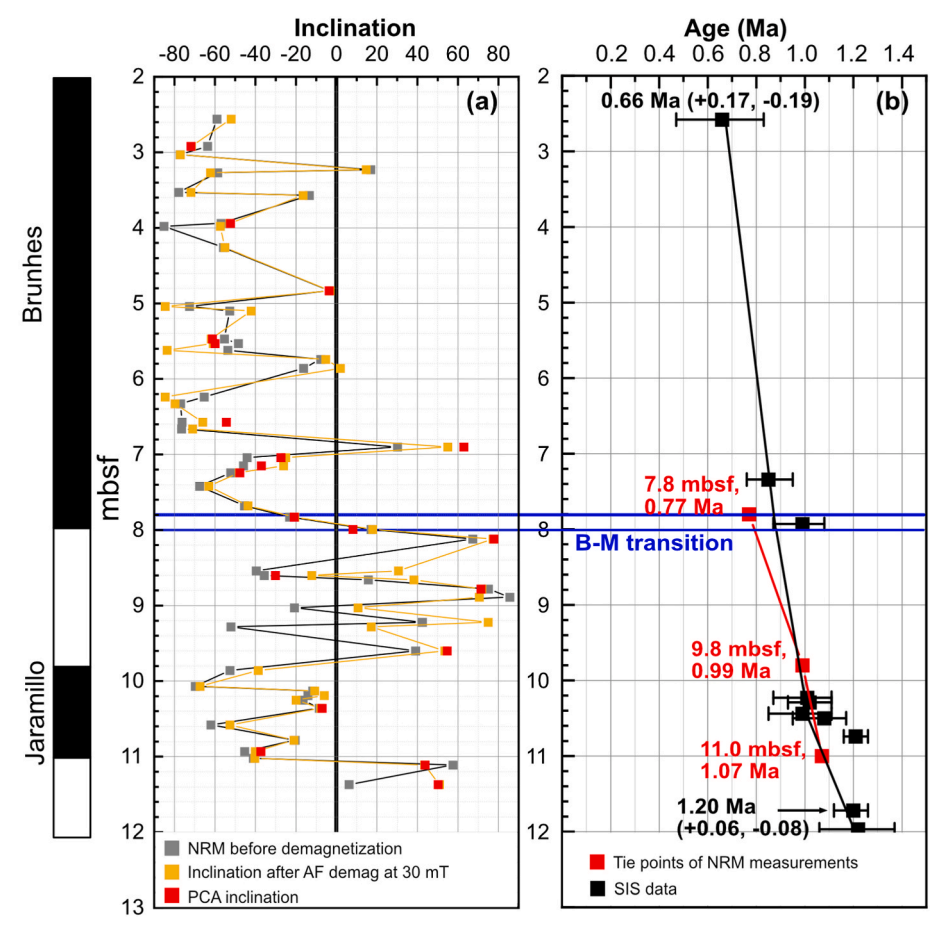
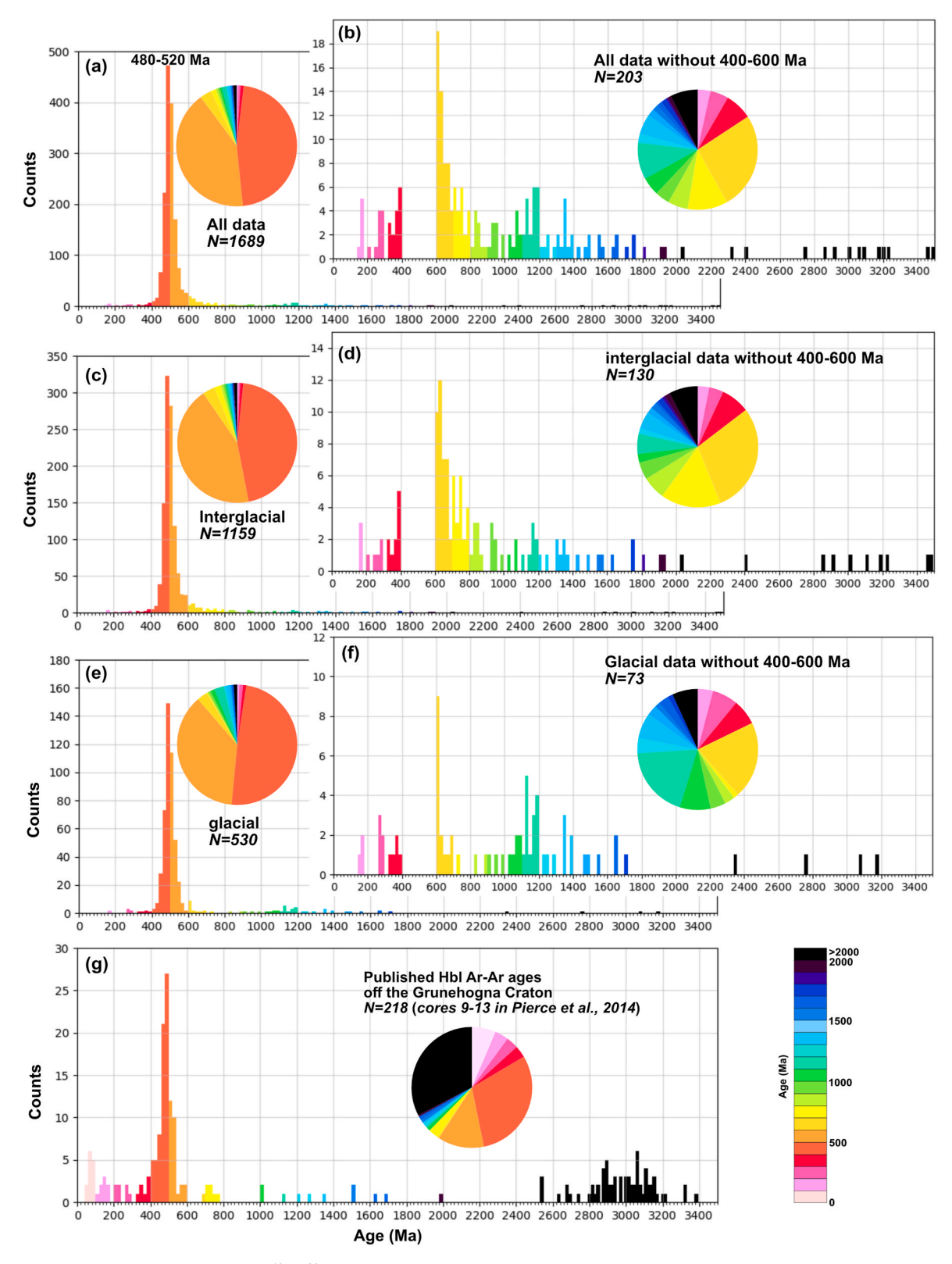


Fig. 3. The downcore variation of NRM measurements and Sr isotope results. (a) Inclination before and after AF demagnetization. The PCA inclination results are mostly based on the measurements of 10–60 mT demagnetization. The data are provided in Supplementary File 3. (b) Age-depth model from Sr isotope stratigraphy and NRM data. Note there appears to be an approximately 100–200 kyr discrepancy at the B-M (Brunhes-Matuyama) boundary.

from the bottom to the top, the core begins with a reversed polarity below 11 mbsf, followed by a normal polarity during 9.8–11 mbsf. A shift to reverse polarity is observed up to 8 mbsf where polarity shifts back to normal (Fig. 3a). Samples with reversed polarity generally

exhibit a greater degree of directional shift during AF demagnetization compared to those with normal polarity, consistent with a steep negative overprint in the present day (Fig. 3a).



**Fig. 4.** Histograms and pie charts of hornblende <sup>40</sup>Ar/<sup>39</sup>Ar ages from DML. (a–b) Complete dataset from this study of ODP Core 693A-2R and the same dataset without 400–600 Ma data. (c–d) The dataset of interglacial sections. (e–f) The dataset of glacial sections. (g) Published hornblende <sup>40</sup>Ar/<sup>39</sup>Ar ages from the sites more proximal to the Grunehogna Craton margin (Pierce et al., 2014, Fig. 1b).

# 4.3. Hornblende 40Ar/39Ar ages

A total of 1689 hornblende grains were analyzed for  $^{40}$ Ar/ $^{39}$ Ar ages (Supplementary File 4). The obtained  $^{40}$ Ar/ $^{39}$ Ar ages from each section of the core are presented in Supplementary Fig. 2. A dominant population of 400–600 Ma (>80%) is present with a significant peak at ca. 520–480 Ma (Fig. 4a). Small populations range from ca. 160 Ma to the Archean ages of ca. 3500 Ma (Fig. 4b).

#### 4.4. IRD concentration and XRF-scanning geochemistry

The down core variations of the weight percentage of >150 μm coarse fraction and its mass accumulation rate (MAR), the abundance of CT-counted IRD (>1 mm), and XRF-derived elemental ratios are shown in Fig. 5a-h, together with the variation in lithology and shipboard measurements of gamma ray attenuation porosity evaluation (GRAPE) bulk density (Barker and Kennett, 1988). The corresponding data for these variations are provided in Supplementary File 5. The >150  $\mu m$ fraction only comprises a small proportion of the sediments generally below 20%. The MAR was calculated with the formula MAR = weight percentage \* dry bulk density (DBD, g/cm<sup>3</sup>)\* linear sedimentation rate (cm/kyr) (McKay et al., 2022). We use a DBD value of 0.8 g/cm<sup>3</sup> here according to Teitler et al. (2015), and we calculate the linear sedimentation rates for different sections of the core (i.e. interglacial and glacial periods). Detailed information and calibration are presented in Tables 2-1 and 2-2 of Supplementary File 5. The weight percentage of the coarse fraction and its MAR generally show a parallel variation (Fig. 5c and d). Specifically, sections with a high concentration of >150  $\mu$ m coarse fraction also exhibit a higher MAR.

IRD abundance correlates well with the physical and geochemical data. Intervals with a high concentration of IRD coincide with increased biogenic versus terrigenous element ratios and higher GRAPE density. The Ba/Al ratio is frequently used as a proxy to deduce changes in paleoproductivity (e.g., Wilson et al., 2018; Hillenbrand et al., 2021), owing to the biogenic nature of Ba, predominantly sourced from Ba-bearing microfossils like radiolarians and diatoms and a primary source of Al from continental rock erosion. An alternative source of Ba, from detrital heavy mineral barite, can be assessed by analyzing the ratio of Ba/Zr. This is because Zr is primarily derived from the detrital heavy mineral zircon, making Zr content a reliable proxy for terrigenous detrital input (Hillenbrand et al., 2021). The concurrent variations in Ba/Al and Ba/Zr ratios negate the possibility of Ba deriving from detrital barite and provide evidence of its biological production. Moreover, the ratios of Ca to terrigenous elements Ti, Fe and Al are indicative of shifts in biogenic calcium carbonate (CaCO<sub>3</sub>) production, primarily from planktonic foraminifera (N. pachyderma). The Si/Ti ratio is used to track changes in biogenic opal content, which represents an indicator of primary productivity in seawater.

#### 5. Discussion

#### 5.1. Age model

With the improved precision and accuracy of Sr isotopic

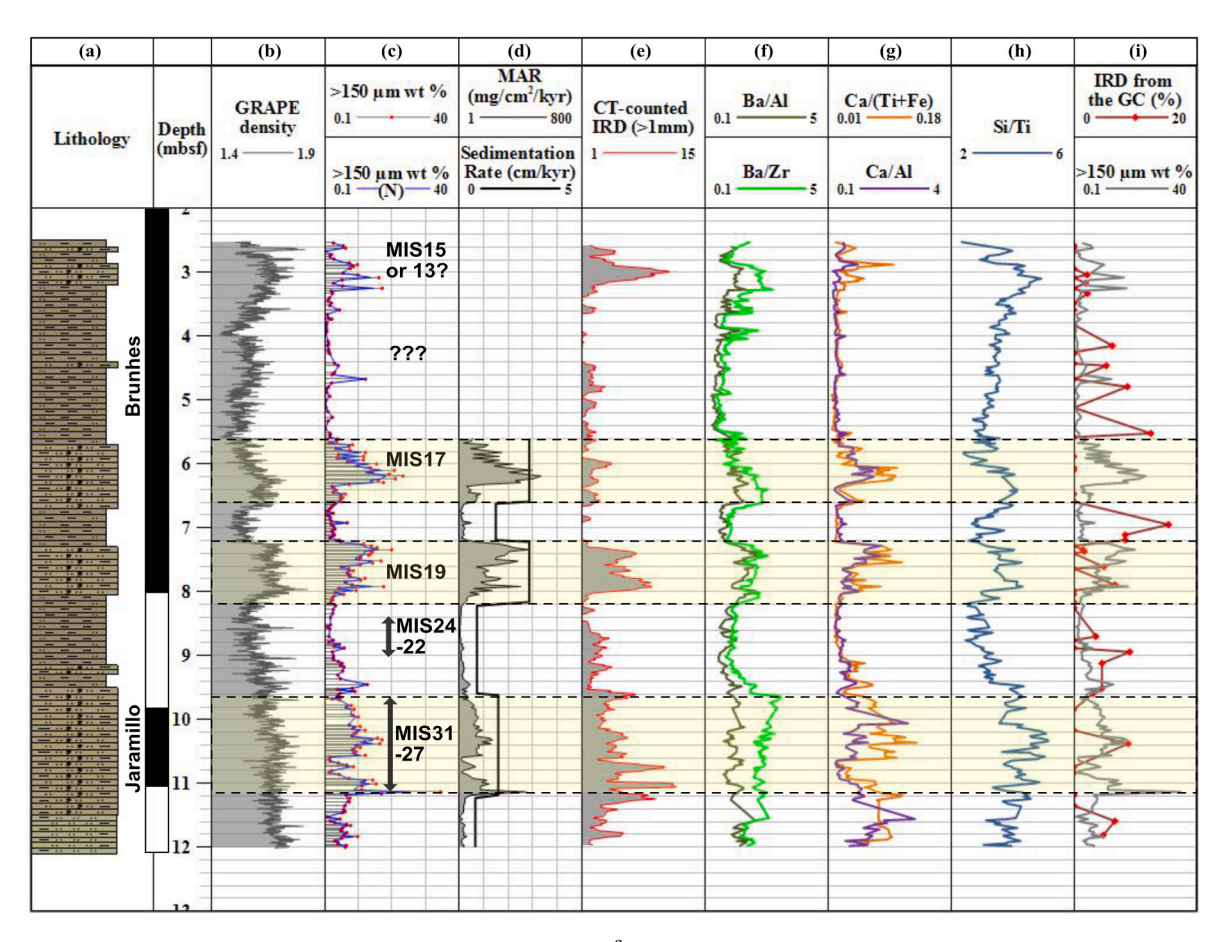


Fig. 5. The down core variation in (a) lithology, (b) GRAPE bulk density (b,  $g/cm^3$ ), (c) weight percentage of >150  $\mu$ m fraction and normalized (N) value, (d) mass accumulation rate (MAR) of >150  $\mu$ m fraction ( $mg/cm^2/kyr$ ) and linear sedimentation rate ( $mg/cm^2/kyr$ ), (e) CT-counted IRD numbers (>1 mm), (f-h) XRF elemental ratios, and (i) the percentage of ice-rafted hornblende grains interpreted to be derived from the Grunehogna Craton (GC, i.e., the percentages of hornblende grains aged 2800–3500 Ma, 1000–1100 Ma, and 160–200 Ma within the total number at each depth, see Section 5.2 for more details) and the weight percentage of >150  $\mu$ m fraction as a comparison.

measurements, as well as the development of the marine Sr-evolution curve (McArthur et al., 2020), Sr isotope stratigraphy has been demonstrated to be a powerful tool to obtain absolute ages and has been widely used in carbonate dating. The well-preserved calcareous foraminifera fossils in the studied core provide excellent subjects for applying Sr isotope dating. However, Sr isotope stratigraphy relies on accurate, high-precision data. The  $2\sigma$  uncertainty of Sr isotopic measurements using modern TIMS may reach as low as  $\pm$  0.000004 (McArthur et al., 2020), but it more commonly falls within the range of  $\pm$ 0.000005–0.000010, resulting in an age uncertainty of 0.1–0.3 Ma for Pleistocene ages. Such levels of age uncertainty could pose considerable challenges in age interpretations, especially when delineating shorter time scales. Hence, within the context of our study, which examines an interval less than 1 Ma, Sr isotopes have been combined with paleomagnetic measurements to obtain a more robust age model.

The results of Sr isotope analyses demonstrate that the studied interval spans the time period 0.65–1.20 Ma (Figs. 2 and 3b), and thus the first geomagnetic reversal at 7.8-8.0 mbsf is believed to correspond to the most recent geomagnetic reversal, the Brunhes-Matuyama reversal. Numerous studies have demonstrated an age of 0.78-0.773 Ma for this reversal (Channell et al., 2020 and references therein). Its duration is interpreted to vary from several to 20-30 thousand years, which has a positive correlation with latitude and becomes protracted in higher-latitude regions (Clement, 2004). In Antarctica, a transitional state with a strong magnetic polarity instability interpreted as the precursors may have persisted for 30 kyr, until the polarity became stable in the present-day field direction at ca. 0.770 Ma (Mahgoub et al., 2023). This interval appears to be represented by the 7.8-8.0 mbsf section in the studied core (Fig. 3b). The interval with a normal magnetic polarity observed at a depth of 9.8-11.0 mbsf corresponds to the Jaramillo normal event, as corroborated by the Sr isotopic ages of 0.99-1.08 Ma from a cluster of four samples at 10.0-10.5 mbsf (Fig. 3b, Table 1). This is consistent with the globally recognized Jaramillo Subchron, which is dated at 1.07 to 0.99 Ma (Channell et al., 2020; Ogg, 2020).

In general, the consistent Sr isotopic age from planktonic foraminifera, when compared with paleomagnetic measurements, has proved the feasibility of using Sr isotope stratigraphy to discriminate short stages, even less than 1 Ma. Nonetheless, the Sr ages obtained from depths of 7.3-8.0 mbsf at 0.85-0.99 Ma are nominally older than the proposed timing of the Brunhes-Matuyama reversal (Fig. 3b). The reason for this age discrepancy is unclear, but it is unlikely to be related to diagenetic alteration or recrystallization of the foraminifera samples. This is because the Sr isotope compositions of recrystallized foraminifera either remain unchanged if altered during sedimentation, or exhibit a greater <sup>87</sup>Sr/<sup>86</sup>Sr ratio than original foraminifera if they interacted with pore water during burial (McArthur et al., 2020). Instead, the discrepancy is more likely attributable to laboratory processes or analytical routines that expose the limitations of high-precision Sr isotope dating. This is also reflected by the age discrepancies in samples from 10 to 11 mbsf, where the sample at 10.74 mbsf appears to be 150 kyr older than the Jaramillo Subchron (Fig. 3b, Table 1). Therefore, this study highlights the importance of conducting multiple analyses of samples from the same depth and combining Sr isotope dating with alternative dating methods to cross-verify the reliability of obtained age information, especially for discriminating short-stage ages. Additionally, another factor potentially contributing to the observed age discrepancy could be the lock-in depth of post-depositional remanent magnetization, which may have resulted in a downward shift of geomagnetic boundaries by 15-20 cm (DeMenocal et al., 1990; Roberts et al., 2013).

The Sr isotopic analyses presented in this study provide, for the first time, a direct age constraint on the Pleistocene sedimentation along the DML continental margin. Mackensen et al. (1989) first attempted to establish a Pleistocene age framework for Core PS1388, located approximately 400 km east of ODP Site 693, using paleomagnetic measurements and by correlating the foraminifera oxygen isotope variations with global isotope stratigraphy. Following this work, Grobe and

Mackensen (1992) examined 11 cores from the DML continental slope spanning 15–5° W and correlated the lithology and isotopic changes of PS1388 with these cores to develop an age model. This model was based on the assumptions of zero age for core tops and constant sedimentation rates between isotopic events, which, however, has not been well substantiated by direct age measurements. In particular, core PS1591, located at the same site as ODP Site 693, was thought to have recorded a 300 kyr sedimentation history in the uppermost 4 m. However, our Sr isotopic results indicate that the uppermost core layer (2.58 mbsf) dates to 0.66 Ma (+0.17, -0.19), suggesting a possible hiatus or an incomplete recovery in the Holocene-late Pleistocene sedimentary records of Core 1.

# 5.2. IRD provenance: insights from hornblende <sup>40</sup>Ar/<sup>39</sup>Ar ages

The ice-rafted hornblende grains from Core 693A-2R show a wide range of 40Ar/39Ar ages spanning from Archean to Jurassic times (Fig. 4a and b), which indicates a diversity of source regions in East Antarctica. As noted in Section 2.2, DML is composed of a set of Archean to Neoproterozoic geological domains assembled during the assembly of Gondwana, with the areas to the east of the Heimefront Shear Zone overprinted by late Neoproterozoic-Cambrian metamorphism (Fig. 1b). To interpret the provenances, it is essential to compare the new hornblende age results with the outcropping DML geology and existing provenance constraints along the DML continental margin (Fig. 1b, Pierce et al., 2014). In addition, both modern observations of iceberg trajectories and provenance studies show that icebergs can travel hundreds to thousands of kilometers before depositing their sediment loads (e.g., Hemming, 2004; Williams et al., 2010; Budge and Long, 2018). In Antarctica, for example, the detritus-carrying icebergs derived from Wilkes Land and Adélie Land have been well known to reach the Prydz Bay region to deposit IRD during the Miocene and Pliocene (Williams et al., 2010; Cook et al., 2014; Pierce et al., 2017). Thus, it is crucial to entertain the possibility that the IRD may have been released by far-traveled icebergs originating from remote locations along the coast of East Antarctica.

Over 80% of all recorded <sup>40</sup>Ar/<sup>39</sup>Ar ages range from 440 to 560 Ma, and the most prominent peak lies at 480–520 Ma (Fig. 4a). This age peak is consistent with a distal source of the IRD from the region of DML that has been subjected to Pan-African tectono-thermal overprint (Fig. 1b). More specifically, the origin of ice-rafted hornblende grains can be correlated to both high-grade metamorphic rocks and late-tectonic granitoids in central-eastern DML. Further east, the Lützow-Holm Bay and Prydz Bay regions have also been overprinted by similar-aged metamorphism (Pierce et al., 2014). We acknowledge the possibility that these regions might have contributed to the ice-rafted hornblende of this period, given the substantial ice front flux from the Amery Ice Shelf (Rignot et al., 2013), and the observed trajectories of modern icebergs showing melting of icebergs derived from Prydz Bay and the regions even further along the coast of DML (Budge and Long, 2018).

A small number of Archean ages, ranging from 2800 to 3500 Ma, have been obtained, with the majority of these ages found in sections older than the Brunhes-Matuyama reversal (Supplementary Fig. 2). In contrast, hornblende  $^{40} \rm Ar/^{39} Ar$  ages previously reported from the continental shelf sediments off the Grunehogna Craton, which likely represent the deposition since the LGM, reveal a significant proportion (~32%) of Archean ages (Fig. 4g). In addition to Archean ages, two other age groups, 1000–1100 Ma and 150–200 Ma, could respectively be attributed to Mesoproterozoic and Jurassic mafic intrusions in the Grunehogna Craton (Fig. 1b).

The Neoproterozoic age group, ranging from 600 to 1000 Ma and constituting approximately 5% of the dataset, was rarely identified in ice-rafted grains from other sectors of East Antarctica (Pierce et al., 2014). Although a small propotion of 600–900 Ma ice-rafted hornblende grains was found in the Prydz Bay region, its origin remains ambiguous (Williams et al., 2010). This age range, however, correlates well with the

geology of central and eastern Dronning Maud Land (DML). The Schirmacher Oasis, located near the coastline of central DML (Fig. 1b), is characterized by magmatism circa 780–750 Ma and 650–600 Ma, coupled with high-grade metamorphism (Jacobs et al., 2020). Additionally, it is distinct from adjacent regions in that it remained unaffected by metamorphism younger than 600 Ma (Jacobs et al., 2020), thus holding significant potential to preserve 40Ar/39Ar ages older than 600 Ma. In eastern DML, despite the pervasive late Neoproterozoic to early Paleozoic tectono-thermal overprinting, a mega-boudin in the southern part of the SW Terrane of the Sør Rondane mountains escaped much of the late Neoproterozoic deformation. This area is characterized by low-grade metamorphism (Fig. 1b, Jacobs et al., 2015), and thus offers potential sources for a variety of 600–1000 Ma hornblende grains.

The provenance of a minor Meso-Paleoproterozoic age group (ca. 1100-1800 Ma) remains ambiguous. The challenging in associating the Grenville-age IRD with the Maud Belt is that the latter has undergone extensive Pan-African metamorphism, and reports of Grenville-age <sup>40</sup>Ar/<sup>39</sup>Ar results from the Maud Belt outcrops are exceedingly rare. To the south of the Grunehogna Craton, the Natal Belt and Coats Land are characterized by Grenville-age basement rocks, mostly unaffected by later Pan-African metamorphism, and exhibit modern glacial-marine sedimentation along their peripheries with a large proportion of 1000-1300 Ma ages (Pierce et al., 2014). However, IRD being derived from these regions seems highly improbable given their position downstream of the Antarctic Coastal Current (ACoC). This is also not supported by observed modern iceberg trajectories within the Weddell Sea. The Ritscherflya Supergroup, as described in Section 2.2, contains 1300-1800 Ma detrital zircons, suggesting a potential for contributing hornblende grains within this age group, although their origins remain unidentified. Another plausible explanation is that the IRD population with 40Ar/39Ar ages of 1100-1800 Ma was primarily melted out of far-traveled icebergs propelled by the westward-flowing ACoC. The Wilkes Land and Adélie sectors are characterized by substantial Meso-Paleoproterozoic sources, and the icebergs calved from there in Miocene times are proposed to have traveled further along the coast of East Antarctica to deposit IRD on the margin of Prydz Bay (Williams et al., 2010; Cook et al., 2014; Pierce et al., 2017).

In summary, our analysis of ice-rafted hornblende 40Ar/39Ar ages suggests that the principal IRD deposited at Site 693 primarily originates from the region to the east of the Grunehogna Craton. Minor IRD contributions may potentially be traced to more distant regions of East Antarctica, extending as far as the Wilkes Land and Adélie sectors. However, the input from the Grunehogna Craton, the closest coastline to Site 693, was found to be minimal. Different bedrock types with distinct compositions and susceptibilities to erosion can introduce biases in provenance records (Cook et al., 2017), and thus it is important to evaluate if the source bedrock is able to contribute to hornblende in the marine sediments. In the case of the Archean granite within the Grunehogna Craton, the investigated outcrops show an absence of hornblende (Marschall et al., 2010). However, this contrasts with the presence of Archean hornblende Ar-Ar ages reported by Pierce et al. (2014), where significant proportions were found in some sites (Fig. 1b). A potential bias in the provenance record is possible for the other two age groups that are associated with the ca. 1000-1100 Ma and 160-200 Ma mafic dykes and sills within the Grunehogna Craton, as the source rocks are primarily doleritic in composition and are notably deficient in hornblende (Riley and Millar, 2014). Considering these age groups collectively, the lack of ice-rafted hornblende derived from the Grunehogna Craton cannot be solely attributed to a source rock bias.

The obtained Ar–Ar results dominated by Pan-African ages are in alignment with the contemporary ice stream patterns in DML, where a series of fast-flowing ice streams developed on the coast of central and eastern DML, which represents an active glacier catchment region (Fig. 1a). Particularly, the Fimbul Ice Shelf, which is fed by fast-flowing Penck Trough and Jutulstraumen ice streams that are sourced from the central and western DML mountains (Fig. 1a), constitutes the largest

glacial catchment in DML. In addition, the sediments from the Jelbart Ice Shelf coast also present a substantial fraction of Pan-African  $^{40}\mathrm{Ar}/^{39}\mathrm{Ar}$  ages and the Archean ages are much fewer than the other cores off the Grunehogna Craton (Fig. 1b). In contrast to these fast-flowing ice streams to the east, ice streams within the Grunehogna Craton exhibit a significantly slower flow velocity, and their estimated calving volume is only one-third of that of the Fimbul Ice Shelf (Fig. 1a, Rignot et al., 2013). In addition, the IRD record from the Grunehogna Craton has been further reduced as icebergs calved off the craton may have traveled equatorward before melting, as indicated by the presence of Archean  $^{40}\mathrm{Ar}/^{39}\mathrm{Ar}$  ages in the IRD deposited in the Scotia Sea at ca. 1.2 Ma (Bailey et al., 2022).

#### 5.3. Glacial-interglacial records: IRD supply and biogenic productivity

Core observations, assisted by X-ray imaging, have revealed a synchronous variation in IRD abundance and foraminifera concentrations (Fig. 5a). Specifically, sections of the core with elevated levels of IRD correspondingly exhibit higher foraminifera concentrations. This pattern of high IRD supply coinciding with increased productivity is further supported by the closely aligned variations in CT-counted IRD quantities and the ratios of Ca to terrigenous elements (Fig. 5e, g), and has also been observed in other late-middle Pleistocene cores off DML (Grobe and Mackensen, 1992; Forsberg et al., 2003). Given the potentially significant impact of sediment winnowing and focusing processes on the continental margin of Antarctica, which preferentially removes fine-grained sediments and concentrates IRD as well as other coarse fractions like biogenic carbonate, sections of the core showing high IRD concentrations might appear to have low IRD accumulation rates and thus could not be interpreted as increased iceberg rafting (e.g., 0 Cofaigh et al., 2001; Teitler et al., 2015). The studied core is dominated by  $< 63 \ \mu m$  fine fraction, which constitutes an average of 95–97% for glacial periods and 85-90% for interglacial periods, while the coarse fraction >150 µm only forms a small proportion of sediments. Here we calculated the normalized values of the weight percentage of  $>150 \mu m$ fraction, considering fine-grained fractions in interglacial periods to be 97%, which are very consistent with the original trend (Fig. 5c). The MARs of coarse fractions in sections of the core that had well-established age constraints (5.6-12 mbsf) have also been calculated. The consistent variation in abundance of coarse fractions and MAR indicates that episodes of increased IRD concentrations during the studied intervals are not likely produced by the winnowing process but can be attributed to episodic iceberg rafting events.

To assess how IRD abundance and accumulation rates evolve during various stages of glacial-interglacial cycles is not straightforward as the deposition and spatial distribution of IRD are controlled by the interplay of multiple contributing factors. The increase in IRD delivery is normally ascribed to increased iceberg discharge associated with the destabilization of outlet glaciers and ice streams, which typically occurs in warming phases (e.g., Williams et al., 2010; Wilson et al., 2018). In Antarctica, elevated IRD deposition has been widely reported during interglacial periods and transitions from glacial to interglacial conditions on the proximal continental margins of various sectors of East Antarctica, including Prydz Bay (Williams and Handwerger, 2005) and Wilkes Land (Escutia et al., 2003; Wilson et al., 2018), as well as the Western Antarctic continental margin in the Bellingshausen Sea (Hillenbrand et al., 2021) and Ross Sea (King et al., 2022). In these sedimentary records, variation in the abundance of IRD has been utilized in conjunction with the patterns of additional climate proxies like XRF-derived elemental ratios indicating biogenic/terrigenous input as a dependable indicator of ice sheet dynamics. For far-traveled icebergs, however, additional factors including SST, sea-ice extent, and ocean circulation patterns can affect iceberg flux by limiting the survival and residence time, consequently altering the location of IRD deposition (Cook et al., 2014; Licht and Hemming, 2017). For example, near the Southern Ocean front towards South Atlantic Ocean, icebergs calved

from the Antarctic margin may have experienced accelerated melting in warmer seawater and open water conditions so that they were not able to reach the distant deposition site, resulting in apparent IRD peaks during glacial periods (Diekmann et al., 2003; Teitler et al., 2015).

The observed peaks in the ratios of Ca to terrigenous elements (Fig. 5g) can be attributed to the prevalence of calcareous foraminifera, predominantly N. pachyderma, which is notably the most abundant planktonic foraminifera in both the Antarctic and Arctic Oceans, as well as their adjacent seas. The peaks in the Si/Ti ratios (Fig. 5h), which are indicative of marine primary productivity, generally precede the peaks in the Ca/Al and Ca/(Ti + Fe) ratios. This suggests that increased primary productivity may have provided the essential nutrients to support the growth of foraminifera.

As noted above, high levels of IRD and biogenic productivity characterize the warm interglacial intervals of the Pleistocene continental margin sedimentation in DML. The observed variability in productivity, coupled with global climate changes, has been similarly documented in late Pleistocene sediments from Wilkes Land and Prydz Bay (Wu et al., 2017; Holder et al., 2020). In these studies, the fluctuations in productivity are primarily linked to variations in nutrient supply, driven by changes in sea ice extent, ice sheet positioning, and deep water circulation patterns. The glacial-interglacial variability in sedimentation and productivity off DML may have been influenced by multiple climate factors including sea level, sea ice and ice shelf disintegration (Grobe and Mackensen, 1992). In addition, deep-water circulation dynamics, particularly the role of the North Atlantic Deep Water (NADW), have played pivotal roles in sedimentation, with a specific impact on carbonate sedimentation in the Southern Ocean (Howard and Prell, 1994). Existing evidence suggests the DML continental shelf has been under the influence of NADW since the middle Pleistocene (Forsberg et al., 2003). An intensified influx of NADW during interglacials could inhibit carbonate dissolution and enhance carbonate preservation, owing to the slight supersaturation of NADW with calcium carbonate (Diekmann, 2007). Therefore, during interglacial periods, rising sea levels and SSTs lead to increased ice sheet melting and iceberg calving at the continental margin, and reduced sea ice increases available light and surface primary productivity, thereby promoting foraminifera concentrations. The influx of NADW further aids in the preservation of foraminifera. The glacial periods, in contrast, are dominated by fine-grained terrigenous sediments, although their provenances are yet to be determined in this study. Evidence from surface sediments shows that the fine-grained terrigenous sediments along DML have been transported by the westward-flowing ACoC (Diekmann and Kuhn, 1999). On the other hand, Site 693 is approximately 10 km southwest of the outer rim of Wegener Canyon, which may have affected the sedimentary environment via gravitational transport and turbidite sedimentation (Grobe et al., 1990). Further provenance studies may help to clarify the local or distal origins of fine-grained sediments.

The cyclical variations in IRD concentration at Site 693 are largely attributed to the ice dynamics in central-eastern DML, as demonstrated by IRD provenance analyses (Section 5.2). Here we attempt to isolate the specific IRD signatures associated with the Grunehogna Craton to understand how the abundance of locally sourced IRD relates to climate fluctuations. All  $^{40}\mathrm{Ar}/^{39}\mathrm{Ar}$  age groups, spanning from the Archean to the Jurassic, are present in both glacial and interglacial sections (Fig. 4a-f). The age groups associated with the Grunehogna Craton do not exhibit variations that align with the patterns of IRD abundance, but instead represent a larger proportion in glacial stages (Fig. 5i). This might be attributable to a diminished contribution of IRD from eastern regions during glacial intervals accentuating the IRD signal from the Grunehogna Craton. Alternatively, it may indicate that ice streams and glaciers within the craton respond to climatic changes in a manner distinct from those in the central-eastern DML, suggesting a complex and nonuniform ice dynamic response to climate changes.

#### 5.4. Implications for ice dynamics in DML during the MPT

The MPT (1.2-0.7 Ma) is characterized by global SST cooling that initiated at 1.2 Ma or even earlier followed by a pronounced cooling at 0.9 Ma (McClymont et al., 2013; Ford and Raymo, 2020). During this period, known as the '900 kyr' event (Clark et al., 2006), the Southern Ocean experienced a northward migration of the polar front by several degrees of latitude (Kemp et al., 2010). Ice volume expansion in Antarctica at ca. 900 ka (MIS 24–22) is indicated by more positive  $\delta^{18}\mathrm{O}$ values in seawater from the Southwest Pacific (Elderfield et al., 2012; Ford and Raymo, 2020) and supported by modeling of the WAIS evolution (Pollard and DeConto, 2009). Evidence from the sedimentary records near Antarctica indicating an expanded ice sheet is mainly reported in the marine-based ice sheet in the Ross Sea, where, for example, sediments recovered by Core AND-1B show a significant unconformity at 1-0.8 Ma with sedimentation characterized by subglacial or grounding-line proximal diamictites (McKay et al., 2012). However, sedimentary records reflecting ice sheet expansion in East Antarctica remain somewhat ambiguous, with only scant evidence from Prydz Bay and DML. From the DML continental margin, planktonic  $\delta^{18}$ O records obtained from Core AN9306-SC1, located approximately 500 km east of Site 693, appear to be more positive after ca. 1.0 Ma (Forsberg et al., 2003), and a similar oxygen isotopic trend has also been reported from Core 1165 off Prydz Bay (Theissen et al., 2003). The ca. 0.9 Ma sedimentary record at Site 693 (MIS 24-22), which is bracketed by an interglacial interval immediately above the Brunhes-Matuyama boundary and a prolonged warming stage of ca. 1.1-1.0 Ma (discussed below), is characterized by low IRD and foraminifera concentrations (Fig. 5). This indicates more stable grounded ice and sea ice presence at the DML continental margin leading into the MPT, which is consistent with the inferred global signal.

Despite the gradual SST cooling during the MPT, this interval includes the noteworthy 'super interglacial' MIS 31 (1.08-1.06 Ma). During this time, the high-latitude Southern Ocean warmed by several degrees above modern-day values (Beltran et al., 2020), potentially leading to the collapse of the WAIS and a reduction in the ice volume and retreat of the EAIS (DeConto et al., 2012). The MIS 31 event is well resolved in sediment cores from the Ross Sea, where it manifests as warmer SSTs than present, greatly reduced sea ice cover, and the deposition of diatomite and carbonate layers (Scherer et al., 2008; McKay et al., 2012; Beltran et al., 2020). A sedimentary sequence consisting of diatomite and volcanic sands with calcareous nannofossils during MIS 31-27 has been interpreted to represent prolonged open water conditions in the Ross Sea (McKay et al., 2012; Villa et al., 2012). In East Antarctica, sedimentary records from the proximal continental margin during this interval are relatively limited. However, the sediment cores at ODP Site 1165 near Prydz Bay show an increased IRD supply and planktonic foraminiferal carbonates associated with more negative  $\delta^{18}\text{O}$  values compared to the subsequent section of post-1 Ma, and the inferred warming stage is estimated to have lasted for approximately 80 kyr, starting from MIS 31 or even MIS 33 (Teitler et al., 2015). Similarly, at Site 693, IRD abundance, the MAR of coarse fractions and biogenic versus terrigenous input are overall elevated with pulses through the Jaramillo Subchron (0.99-1.07 Ma, Fig. 5), apart from a dip to lower Ca versus terrigenous element values from 10.7 to 10.9 mbsf, just above the lower Jaramillo boundary, which may represent MIS 30. These observations suggest that relatively warm conditions may have persisted through most of MIS 31-27 (9.6-11.2 mbsf), characterized by a prolonged retreat of the DML ice sheet, substantial outlet glacier discharge releasing icebergs and increased biogenic productivity. This is comparable to the climate record from the continental margin off Prvdz Bav.

Most of the core section above the Brunhes-Matuyama boundary lacks direct Sr isotope and paleomagnetic constraints, except for the Sr age of 0.66 Ma ( $\pm$ 0.17,  $\pm$ 0.19, n = 3) at 2.58 mbsf. If the glacial-interglacial cyclicity of the studied core above the Brunhes-Matuyama

boundary (at ca. 8 mbsf) is consistent with the approximate 100 kyr cycles of global climate changes (Lisiecki and Raymo, 2005), the well-established age model of the core's lower part offers potential insights into the age range of the upper section. The interval at 7.2-8.2 mbsf, characterized by enhanced IRD abundance and biogenic productivity, is identified as corresponding to MIS 19 (790-755 ka, Lisiecki and Raymo, 2005). The subsequent shifts in IRD and productivity are thus likely to correspond to MIS 18 (6.6-7.2 mbsf, 755-715 ka) and MIS 17 (5.6-6.6 mbsf, 715-680 ka), respectively. Therefore, the implied sedimentation rates during interglacial periods, estimated to be about 3 cm/kyr, are elevated compared to those of glacial stages (Fig. 5d), in line with the previous study of the Pleistocene sedimentation off DML (Grobe and Mackensen, 1992). Accordingly, section (3.4-5.6 mbsf), comprising massive mud with a thin layer of IRD, is more likely to span MIS 16 and MIS 14 (680–535 ka) rather than representing only MIS 16, and the top of the core at 2.5–3.4 mbsf is therefore very likely to represent MIS 13 (535-480 ka), the age of which is still within the range of the Sr isotope results.

In summary, despite challenges in detailed stratigraphy for the late Pleistocene to Holocene sections, the analysis of sedimentological and paleoproductivity variability within Core 693A-2R reveals insights into DML ice dynamics during the MPT. The core captures especially pronounced interglacials of MIS 31 (a 'super-interglacial'), 19 and 17, with substantial instability/break-up of ice shelves leading to the release of icebergs and deposition of IRD. Evidence is also found of a cooling event with ice expansion during MIS 24-22 (the '900 ka event'), although the signs of subsequent ice expansion are limited in the sedimentary record reported here. These findings underscore the need for further investigations on the continental margin sedimentation off DML, focusing particularly on areas closer to the grounding line, to better understand the sedimentation processes and ice sheet history throughout the Pleistocene. Antarctic ice evolution during the MPT has been relatively underexplored, and additional studies on geological records and ice sheet modeling from other sectors of Antarctica will provide broader insights into the AIS dynamics.

#### 6. Conclusions

Sedimentary archives retrieved from the continental slope of the Archean Grunehogna Craton document the history of sediment accumulation and the dynamic responses of DML ice shelves to climate changes across the MPT. An age model is constructed for ODP Core 693A-2R based on Sr isotope stratigraphy of planktonic foraminifera and geomagnetic reversals, indicating that the core spans 1.20-0.65 Ma with an average accumulation rate of 1.5 cm/kyr. The predominant peak of <sup>40</sup>Ar/<sup>39</sup>Ar ages at ca. 520–480 Ma is consistent with the region of DML that has been overprinted by Pan-African metamorphism during the assembly of Gondwana, located several hundred kilometers east of the deposition site. This suggests that the MPT sedimentation at the deposition site correlates more closely with the dynamic evolution of the ice sheet and outlet glaciers in central-eastern DML rather than the most adjacent Grunehogna Craton. The ice shelves in DML were capable of responding sensitively to glacial-interglacial variations in climate and ocean circulation, causing episodic iceberg discharges and IRD deposition associated with enhanced paleoproductivity as evidenced by increased biogenic versus terrigenous input. Ice dynamics in DML, reflecting ice retreat during 1.0–1.1 Ma (MIS 31–27) and subsequent ice advance at ca. 900 ka, are comparable to the available records from other sectors of East Antarctica. In addition to MIS 31-27, interglacial expressions are mainly observed at MIS 19 and 17, which may represent the warm periods with the most dynamic loss of the ice sheet margin due to iceberg calving. This study provides the basis for future studies on glacial-marine sediments off DML and in the Weddell Sea embayment to obtain high-resolution continuous sedimentation records and to better understand the Pleistocene glacier history in East Antarctica.

#### **Author contribution**

Cheng-Cheng Wang: Conceptualization, Methodology, Investigation, Data curation, Writing – original draft, Visualization; Writing – review & editing. Sidney Hemming: Conceptualization, Methodology, Resources, Supervision, Project administration, Funding acquisition; Writing – review & editing. Suzanne O'Connell: Investigation, Resources, Supervision, Data curation. Eliza Carter: Investigation. Troy Rasbury: Investigation, Resources, Data curation. Trevor Williams: Data curation, Visualization, Writing – original draft; Writing – review & editing. Brendan T. Reilly: Software, Data curation, Writing – original draft. Stefanie Brachfeld: Investigation, Resources, Data curation, Funding acquisition. Sanzhong Li: Resources, Supervision

#### **Declaration of competing interest**

The authors declare that they have no known competing financial interests or personal relationships that could have appeared to influence the work reported in this paper.

#### Data availability

I have shared the research data at the Attach File step.

#### Acknowledgments

This study was financially supported by the U.S. National Science Foundation Office of Polar Programs under grants OPP/ANT No. 1342213 and No. 1342000 as well as additional grants from the Columbia Climate Center. We thank Tanzhuo Liu for help with <sup>40</sup>Ar/<sup>39</sup>Ar analyses, Katie Wooton for help with Sr isotopic analyses and Stephen Cox for his help with CT imaging. We also thank the shipboard scientific party and crews of ODP Leg 113. Finally, we would like to thank all the reviewers for their constructive and encouraging feedback, which has strengthened the manuscript.

#### Appendix A. Supplementary data

Supplementary data to this article can be found online at https://doi.org/10.1016/j.quascirev.2023.108483.

## References

- Andersen, J.L., Newall, J.C., Blomdin, R., Sams, S.E., Fabel, D., Koester, A.J., Lifton, N.A., Fredin, O., Caffee, M.W., Glasser, N.F., Rogozhina, I., 2020. Ice surface changes during recent glacial cycles along the Jutulstraumen and Penck Trough ice streams in western Dronning Maud Land, East Antarctica. Quat. Sci. Rev. 249, 106636 https://doi.org/10.1016/j.quascirev.2020.106636.
- Bailey, I., Hemming, S., Reilly, B.T., Rollinson, G., Williams, T., Weber, M.E., Raymo, M. E., Peck, V.L., Ronge, T.A., Brachfeld, S., O'Connell, S., 2022. Episodes of early Pleistocene West Antarctic ice sheet retreat recorded by iceberg Alley sediments. Paleoceanogr. Paleoclimatol. 37 (7), e2022PA004433 https://doi.org/10.1029/2022PA004433
- Proceedings of the Ocean Drilling Program, 113 initial reports. In: Barker, P.E., Kennett, J.P. (Eds.), 1988. Proceedings of the Ocean Drilling Program. Ocean Drilling Program, College Station, Texas. https://doi.org/10.2973/odp.proc. ir 113 1988
- Barker, S., Greaves, M., Elderfield, H., 2003. A study of cleaning procedures used for foraminiferal Mg/Ca paleothermometry. G-cubed 4 (9). https://doi.org/10.1029/ 2003GC000559.
- Beltran, C., Golledge, N.R., Ohneiser, C., Kowalewski, D.E., Sicre, M.A., Hageman, K.J., Smith, R., Wilson, G.S., Mainié, F., 2020. Southern Ocean temperature records and ice-sheet models demonstrate rapid Antarctic ice sheet retreat under low atmospheric CO<sub>2</sub> during Marine Isotope Stage 31. Quat. Sci. Rev. 228, 106069 https://doi.org/10.1016/j.quascirev.2019.106069.
- Budge, J.S., Long, D.G., 2018. A comprehensive database for Antarctic iceberg tracking using scatterometer data. IEEE J. Sel. Top. Appl. Earth Obs. Rem. Sens. 11 (2), 434–442. https://doi.org/10.1109/JSTARS.2017.2784186.
- Channell, J.E., Singer, B.S., Jicha, B.R., 2020. Timing of Quaternary geomagnetic reversals and excursions in volcanic and sedimentary archives. Quat. Sci. Rev. 228, 106114 https://doi.org/10.1016/j.quascirev.2019.106114.
- Clark, P.U., Archer, D., Pollard, D., Blum, J.D., Rial, J.A., Brovkin, V., Mix, A.C., Pisias, N. G., Roy, M., 2006. The middle Pleistocene transition: characteristics, mechanisms,

- and implications for long-term changes in atmospheric pCO2. Quat. Sci. Rev. 25 (23–24), 3150–3184. https://doi.org/10.1016/j.quascirev.2006.07.008.
- Clement, B.M., 2004. Dependence of the duration of geomagnetic polarity reversals on site latitude. Nature 428 (6983), 637–640. https://doi.org/10.1038/nature02459.
- Cook, C.P., Hill, D.J., van de Flierdt, T., Williams, T., Hemming, S.R., Dolan, A.M., Pierce, E.L., Escutia, C., Harwood, D., Cortese, G., Gonzales, J.J., 2014. Sea surface temperature control on the distribution of far-traveled Southern Ocean ice-rafted detritus during the Pliocene. Paleoceanography 29 (6), 533–548. https://doi.org/ 10.1002/2014PA002625.
- Cook, C.P., Hemming, S.R., van de Flierdt, T., Davis, E.L.P., Williams, T., Galindo, A.L., Jimenez-Espejo, F.J., Escutia, C., 2017. Glacial erosion of East Antarctica in the Pliocene: a comparative study of multiple marine sediment provenance tracers. Chem. Geol. 466, 199–218. https://doi.org/10.1016/j.chemgeo.2017.06.011.
- DeConto, R.M., Pollard, D., Kowalewski, D., 2012. Reprint of: modeling Antarctic ice sheet and climate variations during marine isotope stage 31. Global Planet. Change 96, 181–188. https://doi.org/10.1016/j.gloplacha.2012.05.018.
- DeMenocal, P.B., Ruddiman, W.F., Kent, D.V., 1990. Depth of post-depositional remanence acquisition in deep-sea sediments: a case study of the Brunhes-Matuyama reversal and oxygen isotopic Stage 19.1. Earth Planet Sci. Lett. 99 (1–2), 1–13. https://doi.org/10.1016/0012-821X(90)90066-7.
- Diekmann, B., Kuhn, G., 1999. Provenance and dispersal of glacial-marine surface sediments in the Weddell Sea and adjoining areas, Antarctica: ice-rafting versus current transport. Mar. Geol. 158 (1-4), 209-231. https://doi.org/10.1016/S0025-3227(98)00165-0.
- Diekmann, B., Fütterer, D.K., Grobe, H., Hillenbrand, C.D., Kuhn, G., Michels, K., Petschick, R., Pirrung, M., 2003. Terrigenous sediment supply in the polar to temperate South Atlantic: land-ocean links of environmental changes during the late Quaternary. In: Wefer, G., Mulitza, S., Ratmeyer, V. (Eds.), The South Atlantic in the late Quaternary: Reconstruction of material budgets and current systems. Springer-Verlag, Berlin Heidelberg New York Tokyo, pp. 375–399.
- Diekmann, B., 2007. Sedimentary patterns in the late quaternary Southern Ocean. Deep Sea Res. Part II Top. Stud. Oceanogr. 54 (21–22), 2350–2366. https://doi.org/ 10.1016/j.dsr2.2007.07.025.
- Ebbing, J., Dilixiati, Y., Haas, P., Ferraccioli, F., Scheiber-Enslin, S., 2021. East Antarctica magnetically linked to its ancient neighbours in Gondwana. Sci. Rep. 11 (1), 1–11. https://doi.org/10.1038/s41598-021-84834-1.
- Elburg, M.A., Andersen, T., Jacobs, J., Läufer, A., Ruppel, A., Krohne, N., Damaske, D., 2016. One hundred fifty million years of intrusive activity in the Sør Rondane Mountains (East Antarctica): implications for Gondwana assembly. J. Geol. 124 (1), 1–26. https://doi.org/10.1086/684052.
- Elderfield, H., Ferretti, P., Greaves, M., Crowhurst, S., McCave, I.N., Hodell, D., Piotrowski, A.M., 2012. Evolution of ocean temperature and ice volume through the mid-Pleistocene climate transition. Science 337 (6095), 704–709. https://doi.org/ 10.1126/science.1221294.
- Escutia, C., Warnke, D., Acton, G.D., Barcena, A., Burckle, L., Canals, M., Frazee, C.S., 2003. Sediment distribution and sedimentary processes across the Antarctic Wilkes land margin during the quaternary. Deep Sea Res. Part II Top. Stud. Oceanogr. 50 (8–9), 1481–1508. https://doi.org/10.1016/S0967-0645(03)00073-0.
- Ford, H.L., Raymo, M.E., 2020. Regional and global signals in seawater δ18O records across the mid-Pleistocene transition. Geology 48 (2), 113–117. https://doi.org/ 10.1130/G46546.1
- Forsberg, C.F., Løvlie, R., Jansen, E., Solheim, A., Sejrup, H.P., Lie, H.E., 2003. A 1.3-Myr palaeoceanographic record from the continental margin off Dronning Maud Land, Antarctica. Palaeogeogr. Palaeoclimatol. Palaeoecol. 198 (1–2), 223–235. https://doi.org/10.1016/S0031-0182(03)00402-4.
- Grantham, G.H., Elburg, M.A., Ueckermann, H., Iaccheri, L., Ngobeli, R., Moabi, N.G., 2023. The age and chemistry of granitic gneisses from the western HU Sverdrupfjella, Maud Terrane, western Dronning Maud Land, Antarctica. Lithos 444, 107128. https://doi.org/10.1016/j.lithos.2023.107128.
- Grobe, H., Fütterer, D., Spiess, V., 1990. Oligocene to quaternary sedimentation processes on the Antarctic continental margin, ODP Leg 113, site 693. In: Proceedings of the Ocean Drilling Program. Scientific Results, pp. 121–131. https://doi.org/10.2973/odp.proc.sr.113.193.1990, 113.
- Grobe, H., Mackensen, A., 1992. Late Quaternary climatic cycles as recorded in sediments from the Antarctic continental margin. The Antarctic paleoenvironment: A perspective on Global Change; Antarctic Research Series 56, 349–376.
- Golledge, N.R., Levy, R.H., McKay, R.M., Naish, T.R., 2017. East Antarctic ice sheet most vulnerable to Weddell Sea warming. Geophys. Res. Lett. 44 (5), 2343–2351. https://doi.org/10.1002/2016GL072422.
- Golynsky, A.V., Ferraccioli, F., Hong, J.K., Golynsky, D.A., von Frese, R.R.B., Young, D. A., Blankenship, D.D., Holt, J.W., Ivanov, S.V., Kiselev, A.V., Masolov, V.N., 2018. New magnetic anomaly map of the Antarctic. Geophys. Res. Lett. 45 (13), 6437–6449. https://doi.org/10.1029/2018GL078153.
- Gulick, S.P., Shevenell, A.E., Montelli, A., Fernandez, R., Smith, C., Warny, S., Bohaty, S. M., Sjunneskog, C., Leventer, A., Frederick, B., Blankenship, D.D., 2017. Initiation and long-term instability of the East Antarctic ice sheet. Nature 552 (7684), 225–229. https://doi.org/10.1038/nature25026.
- Hanson, R.E., Harmer, R.E., Blenkinsop, T.G., Bullen, D.S., Dalziel, I.W.D., Gose, W.A., Hall, R.P., Kampunzu, A.B., Key, R.M., Mukwakwami, J., Munyanyiwa, H., 2006. Mesoproterozoic intraplate magmatism in the Kalahari Craton: a review. J. Afr. Earth Sci. 46 (1–2), 141–167. https://doi.org/10.1016/j.jafrearsci.2006.01.016.
- Hemming, S.R., 2004. Heinrich events: massive late Pleistocene detritus layers of the North Atlantic and their global climate imprint. Rev. Geophys. 42 (1) https://doi. org/10.1029/2003RG000128.
- Hillenbrand, C.D., Crowhurst, S.J., Williams, M., Hodell, D.A., McCave, I.N., Ehrmann, W., Xuan, C., Piotrowski, A.M., Hernández-Molina, F.J., Graham, A.G.C.,

- Grobe, H., Williams, T.J., Horrocks, J.R., Allen, C.S., Larter, R.D., 2021. New insights from multi-proxy data from the West Antarctic continental rise: implications for dating and interpreting Late Quaternary palaeoenvironmental records. Quat. Sci. Rev. 257, 106842 https://doi.org/10.1016/j.quascirev.2021.106842.
- Holder, L., Duffy, M., Opdyke, B., Leventer, A., Post, A., O'Brien, P., Armand, L.K., 2020. Controls since the mid-Pleistocene transition on sedimentation and primary productivity downslope of Totten Glacier, East Antarctica. Paleoceanogr. Paleoclimatol. 35 (12), e2020PA003981 https://doi.org/10.1029/2020PA003981.
- Howard, W.R., Prell, W.L., 1994. Late Quaternary CaCO3 production and preservation in the Southern Ocean: implications for oceanic and atmospheric carbon cycling. Paleoceanography 9 (3), 453–482. https://doi.org/10.1029/93PA03524.
- Huang, X., Jokat, W., 2016. Middle Miocene to present sediment transport and deposits in the Southeastern Weddell Sea, Antarctica. Global Planet. Change 139, 211–225. https://doi.org/10.1016/j.gloplacha.2016.03.002.
- Jacobs, J., Fanning, C.M., Henjes-Kunst, F., Olesch, M., Paech, H.J., 1998. Continuation of the Mozambique Belt into East Antarctica: Grenville-age metamorphism and polyphase pan-African high-grade events in central Dronning Maud land. J. Geol. 106 (4), 385–406. https://doi.org/10.1086/516031.
- Jacobs, J., Thomas, R.J., 2004. Himalayan-type indenter-escape tectonics model for the southern part of the late Neoproterozoic-early Paleozoic East African-Antarctic orogen. Geology 32 (8), 721–724. https://doi.org/10.1130/G20516.1.
- Jacobs, J., Elburg, M., Läufer, A., Kleinhanns, I.C., Henjes-Kunst, F., Estrada, S., Ruppel, A.S., Damaske, D., Montero, P., Bea, F., 2015. Two Distinct Late Mesoproterozoic/early Neoproterozoic Basement Provinces in Central/eastern Dronning Maud Land, East Antarctica: the Missing Link, 15–21, vol. 265. E. Precambrian Research, pp. 249–272. https://doi.org/10.1016/j. precamres.2015.05.003.
- Jacobs, J., Mikhalsky, E., Henjes-Kunst, F., Läufer, A., Thomas, R.J., Elburg, M.A., Wang, C.C., Estrada, S., Skublov, S., 2020. Neoproterozoic geodynamic evolution of easternmost Kalahari: constraints from U-Pb-Hf-O zircon, Sm-Nd isotope and geochemical data from the Schirmacher Oasis, East Antarctica. Precambrian Res. 342, 105553 https://doi.org/10.1016/j.precampres.2019.105553.
- Kemp, A.E.S., Grigorov, I., Pearce, R.B., Garabato, A.N., 2010. Migration of the Antarctic Polar Front through the mid-Pleistocene transition: evidence and climatic implications. Quat. Sci. Rev. 29 (17–18), 1993–2009. https://doi.org/10.1016/j. guascirev.2010.04.027.
- King, M.V., Gales, J.A., Laberg, J.S., McKay, R.M., De Santis, L., Kulhanek, D.K., Hosegood, P.J., Morris, A., Expedition, I.O.D.P., 2022. Pleistocene depositional environments and links to cryosphere-ocean interactions on the eastern Ross Sea continental slope, Antarctica (IODP Hole U1525A). Mar. Geol. 443, 106674 https:// doi.org/10.1016/j.margeo.2021.106674.
- Kirschvink, J., 1980. The least-squares line and plane and the analysis of palaeomagnetic data. Geophys. J. Int. 62 (3), 699–718. https://doi.org/10.1111/j.1365-246X.1980.
- Kuiper, K.F., Deino, A., Hilgen, F.J., Krijgsman, W., Renne, P.R., Wijbrans, A.J., 2008. Synchronizing rock clocks of Earth history. Science 320 (5875), 500–504. https://doi.org/10.1126/science.1154339.
- Lee, J.Y., Marti, K., Severinghaus, J.P., Kawamura, K., Yoo, H.S., Lee, J.B., Kim, J.S., 2006. A redetermination of the isotopic abundances of atmospheric Ar. Geochem. Cosmochim. Acta 70 (17), 4507–4512. https://doi.org/10.1016/j.gca.2006.06.1563
- Licht, K.J., Hemming, S.R., 2017. Analysis of Antarctic glacigenic sediment provenance through geochemical and petrologic applications. Quat. Sci. Rev. 164, 1–24. https:// doi.org/10.1016/j.guascirev.2017.03.009.
- Lisiecki, L.E., Raymo, M.E., 2005. A Pliocene-Pleistocene stack of 57 globally distributed benthic δ18O records. Paleoceanography 20 (1). https://doi.org/10.1029/ 2004PA001071.
- Livingstone, S.J., Ó Cofaigh, C., Stokes, C.R., Hillenbrand, C.D., Vieli, A., Jamieson, S.S., 2012. Antarctic palaeo-ice streams. Earth Sci. Rev. 111 (1–2), 90–128. https://doi. org/10.1016/j.earscirev.2011.10.003.
- Loewy, S.L., Dalziel, I.W.D., Pisarevsky, S., Connelly, J.N., Tait, J., Hanson, R.E., Bullen, D., 2011. Coats Land crustal block, East Antarctica: a tectonic tracer for Laurentia? Geology 39 (9), 859–862. https://doi.org/10.1130/G32029.1.
- Mackensen, A., Grobe, H., Hubberten, H.W., Spiess, V., Fütterer, D.K., 1989. Stable isotope stratigraphy from the Antarctic continental margin during the last one million years. Mar. Geol. 87 (2–4), 315–321. https://doi.org/10.1016/0025-3227 (89)90068-6
- Mahgoub, A.N., Korte, M., Panovska, S., 2023. Characteristics of the Matuyama-Brunhes magnetic field reversal based on a global data compilation. J. Geophys. Res. Solid Earth 128 (2), e2022JB025286. https://doi.org/10.1029/2022JB025286.
- Marschall, H.R., Hawkesworth, C.J., Storey, C.D., Dhuime, B., Leat, P.T., Meyer, H.P., Tamm-Buckle, S., 2010. The annandagstoppane granite, East Antarctica: evidence for archaean intracrustal recycling in the kaapvaal–grunehogna craton from zircon O and Hf isotopes. J. Petrol. 51 (11), 2277–2301. https://doi.org/10.1093/petrology/egq057.
- Marschall, H.R., Hawkesworth, C.J., Leat, P.T., 2013. Mesoproterozoic subduction under the eastern edge of the kalahari-grunehogna craton preceding rodinia assembly: the Ritscherflya detrital zircon record, ahlmannryggen (dronning Maud land, Antarctica). Precambrian Res. 236, 31–45. https://doi.org/10.1016/j. precamres.2013.07.006.
- Mas e Braga, M., Jones, R.S., Bernales, J., Andersen, J.L., Fredin, O., Morlighem, M., Koester, A.J., Lifton, N.A., Harbor, J.M., Suganuma, Y., Glasser, N.F., Rogozhina, I., Stroeven, A.P., 2023. A thicker Antarctic ice stream during the mid-Pliocene warm period. Communications Earth & Environment 4 (1), 321. https://doi.org/10.1038/s43347.073.00983.3

- Matsuoka, K., Skoglund, A., Roth, G., de Pomereu, J., Griffiths, H., Headland, R., Herried, B., Katsumata, K., Le Brocq, A., Licht, K., Morgan, F., 2021. Quantarctica, an integrated mapping environment for Antarctica, the Southern Ocean, and sub-Antarctic islands. Environ. Model. Software 140, 105015. https://doi.org/10.1016/j. envsoft.2021.105015.
- McArthur, J.M., Howarth, R.J., Shields, G.A., Zhou, Y., 2020. Strontium isotope stratigraphy. In: Geologic Time Scale 2020. Elsevier, pp. 211–238. https://doi.org/ 10.1016/B978-0-12-824360-2.00007-3.
- McClymont, E.L., Sosdian, S.M., Rosell-Melé, A., Rosenthal, Y., 2013. Pleistocene seasurface temperature evolution: early cooling, delayed glacial intensification, and implications for the mid-Pleistocene climate transition. Earth Sci. Rev. 123, 173–193. https://doi.org/10.1016/j.earscirev.2013.04.006.
- McKay, R., Naish, T., Powell, R., Barrett, P., Scherer, R., Talarico, F., Kyle, P., Monien, D., Kuhn, G., Jackolski, C., Williams, T., 2012. Pleistocene variability of Antarctic ice sheet extent in the Ross embayment. Quat. Sci. Rev. 34, 93–112. https://doi.org/10.1016/j.quascirev.2011.12.012.
- McKay, R., Albot, O., Dunbar, G.B., Lee, J.I., Lee, M.K., Yoo, K.C., Kim, S., Turton, N., Kulhanek, D., Patterson, M., Levy, R., 2022. A comparison of methods for identifying and quantifying ice rafted debris on the Antarctic margin. Paleoceanogr. Paleoclimatol. 37 (4), e2021PA004404 https://doi.org/10.1029/2021PA004404.
- Min, K., Mundil, R., Renne, P.R., Ludwig, K.R., 2000. A test for systematic errors in 40Ar/39Ar geochronology through comparison with U/Pb analysis of a 1.1-Ga rhyolite. Geochem. Cosmochim. Acta 64 (1), 73–98. https://doi.org/10.1016/S0016-7037 (99)00204-5.
- Ó Cofaigh, C., Dowdeswell, J.A., Pudsey, C.J., 2001. Late quaternary iceberg rafting along the antarctic peninsula continental rise and in the Weddell and Scotia seas. Quat. Res. 56 (3), 308–321. https://doi:10.1006/qres.2001.2267.
- Ogg, J.G., 2020. Geomagnetic polarity time scale. In: Geologic Time Scale 2020. Elsevier, pp. 159–192. https://doi.org/10.1016/B978-0-12-824360-2.00005-X.
- Pierce, E.L., Hemming, S.R., Williams, T., Van de Flierdt, T., Thomson, S.N., Reiners, P. W., Gehrels, G.E., Brachfeld, S.A., Goldstein, S.L., 2014. A comparison of detrital U-Pb zircon, 40Ar/39Ar hornblende, 40Ar/39Ar biotite ages in marine sediments off East Antarctica: implications for the geology of subglacial terrains and provenance studies. Earth Sci. Rev. 138, 156–178. https://doi.org/10.1016/j.earscirev.2014.08.010.
- Pierce, E.L., van de Flierdt, T., Williams, T., Hemming, S.R., Cook, C.P., Passchier, S., 2017. Evidence for a dynamic East Antarctic ice sheet during the mid-Miocene climate transition. Earth Planet Sci. Lett. 478, 1–13. https://doi.org/10.1016/j. epsl.2017.08.011.
- Pollard, D., DeConto, R.M., 2009. Modelling West Antarctic ice sheet growth and collapse through the past five million years. Nature 458 (7236), 329–332. https:// doi.org/10.1038/nature07809.
- Raymo, M.E., Lisiecki, L.E., Nisancioglu, K.H., 2006. Plio-Pleistocene ice volume, Antarctic climate, and the global δ18O record. Science 313 (5786), 492–495. https://doi.org/10.1126/science.1123296.
- Reilly, B.T., Stoner, J.S., Mix, A.C., Walczak, M.H., Jennings, A., Jakobsson, M., Dyke, L., Glueder, A., Nicholls, K., Hogan, K.A., Mayer, L.A., 2019. Holocene break-up and reestablishment of the petermann ice tongue, northwest Greenland. Quat. Sci. Rev. 218, 322–342. https://doi.org/10.1016/j.quascirev.2019.06.023.Rignot, E., Jacobs, S., Mouginot, J., Scheuchl, B., 2013. Ice-shelf melting around
- Rignot, E., Jacobs, S., Mouginot, J., Scheuchl, B., 2013. Ice-shelf melting around Antarctica. Science 341 (6143), 266–270. https://doi.org/10.1126/ science.1235798.
- Rignot, E., Mouginot, J., Scheuchl, B., 2017. MEaSUREs inSAR-Based Antarctica Ice Velocity Map, Version 2. NASA National Snow and Ice Data Center Distributed Active Archive Center, Boulder, Colorado USA. https://doi.org/10.5067/ IKBWW4RYHFIO.
- Riley, T.R., Leat, P.T., Curtis, M.L., Millar, I.L., Duncan, R.A., Fazel, A., 2005. Early–Middle Jurassic dolerite dykes from Western Dronning Maud Land (Antarctica): identifying mantle sources in the Karoo large igneous province. J. Petrol. 46 (7), 1489–1524. https://doi.org/10.1093/petrology/egi023.
- Riley, T.R., Millar, I.L., 2014. Geochemistry of the 1100 Ma intrusive rocks from the ahlmannryggen region, dronning Maud land, Antarctica. Antarct. Sci. 26 (4), 389–399. https://doi.org/10.1017/S0954102013000916.
- Roberts, A.P., Tauxe, L., Heslop, D., 2013. Magnetic paleointensity stratigraphy and high-resolution Quaternary geochronology: successes and future challenges. Quat. Sci. Rev. 61, 1–16. https://doi.org/10.1016/j.quascirev.2012.10.036.

- Ruppel, A.S., Jacobs, J., Läufer, A., Ratschbacher, L., Pfänder, J.A., Sonntag, B.L., Krasniqi, K., Elburg, M., Krohne, N., Damaske, D., Lisker, F., 2021. Protracted late Neoproterozic–early Palaeozoic deformation and cooling history of Sør Rondane, East Antarctica, from 40Ar/39Ar and U–Pb geochronology. Geol. Mag. 158 (4), 635–655. https://doi.org/10.1017/S0016756820000746.
- Scherer, R.P., Bohaty, S.M., Dunbar, R.B., Esper, O., Flores, J.A., Gersonde, R., Harwood, D.M., Roberts, A.P., Taviani, M., 2008. Antarctic records of precessionpaced insolation-driven warming during early Pleistocene Marine Isotope Stage 31. Geophys. Res. Lett. 35 (3) https://doi.org/10.1029/2007GL032254.
- Stokes, C.R., Abram, N.J., Bentley, M.J., Edwards, T.L., England, M.H., Foppert, A., Jamieson, S.S., Jones, R.S., King, M.A., Lenaerts, J.T., Medley, B., 2022. Response of the East antarctic ice sheet to past and future climate change. Nature 608 (7922), 275–286. https://doi.org/10.1038/s41586-022-04946-0.
- Suganuma, Y., Kaneda, H., Mas e Braga, M., Ishiwa, T., Koyama, T., Newall, J.C., Okuno, J.I., Obase, T., Saito, F., Rogozhina, I., Andersen, J.L., 2022. Regional sealevel highstand triggered Holocene ice sheet thinning across coastal Dronning Maud Land, East Antarctica. Communications Earth & Environment 3 (1), 273. https://doi. org/10.1038/s43247-022-00599-z.
- Sutter, J., Fischer, H., Grosfeld, K., Karlsson, N.B., Kleiner, T., Van Liefferinge, B., Eisen, O., 2019. Modelling the antarctic ice sheet across the mid-pleistocene transition-implications for oldest ice. Cryosphere 13 (7), 2023–2041. https://doi. org/10.5194/tc-13-2023-2019.
- Teitler, L., Florindo, F., Warnke, D.A., Filippelli, G.M., Kupp, G., Taylor, B., 2015.
  Antarctic Ice Sheet response to a long warm interval across Marine Isotope Stage 31:
  a cross-latitudinal study of iceberg-rafted debris. Earth Planet Sci. Lett. 409,
  109–119. https://doi.org/10.1016/j.epsl.2014.10.037.
- Theissen, K.M., Dunbar, R.B., Cooper, A.K., Mucciarone, D.A., Hoffmann, D., 2003. The Pleistocene evolution of the East antarctic ice sheet in the Prydz Bay region: stable isotopic evidence from ODP site 1167. Global Planet. Change 39 (3–4), 227–256. https://doi.org/10.1016/S0921-8181(03)00118-8.
- Villa, G., Persico, D., Wise, S.W., Gadaleta, A., 2012. Calcareous nannofossil evidence for Marine Isotope Stage 31 (1 Ma) in core AND-1B, ANDRILL McMurdo ice shelf project (Antarctica). Global Planet. Change 96, 75–86. https://doi.org/10.1016/j. gloplacha.2009.12.003.
- Wang, C.-C., Jacobs, J., Elburg, M.A., Läufer, A., Thomas, R.J., Elvevold, S., 2020a. Grenville-age continental arc magmatism and crustal evolution in central Dronning Maud Land (East Antarctica): zircon geochronological and Hf–O isotopic evidence. Gondwana Res. 82, 108–127. https://doi.org/10.1016/j.gr.2019.12.004.
- Wang, C.-C., Jacobs, J., Elburg, M.A., Läufer, A., Elvevold, S., 2020b. Late neoproterozoic–cambrian magmatism in dronning Maud land (East Antarctica): U–Pb zircon geochronology, isotope geochemistry and implications for Gondwana assembly. Precambrian Res. 350, 105880 https://doi.org/10.1016/j. precamres.2020.105880.
- Will, T.M., Frimmel, H.E., Zeh, A., Le Roux, P., Schmädicke, E., 2010. Geochemical and isotopic constraints on the tectonic and crustal evolution of the Shackleton Range, East Antarctica, and correlation with other Gondwana crustal segments. Precambrian Res. 180 (1–2), 85–112. https://doi.org/10.1016/j. precampres 2010 03 005
- Williams, T., Handwerger, D., 2005. A high-resolution record of early Miocene Antarctic glacial history from ODP Site 1165, Prydz Bay. Paleoceanography 20 (2). https:// doi.org/10.1029/2004PA001067.
- Williams, T., van de Flierdt, T., Hemming, S.R., Chung, E., Roy, M., Goldstein, S.L., 2010. Evidence for iceberg armadas from East Antarctica in the Southern Ocean during the late Miocene and early Pliocene. Earth Planet Sci. Lett. 290 (3–4), 351–361. https://doi.org/10.1016/j.epsl.2009.12.031.
- Wilson, D.J., Bertram, R.A., Needham, E.F., van de Flierdt, T., Welsh, K.J., McKay, R.M., Mazumder, A., Riesselman, C.R., Jimenez-Espejo, F.J., Escutia, C., 2018. Ice loss from the East antarctic ice sheet during late Pleistocene interglacials. Nature 561 (7723), 383–386. https://doi.org/10.1038/s41586-018-0501-8.
- Wu, L., Wang, R., Xiao, W., Ge, S., Chen, Z., Krijgsman, W., 2017. Productivity-climate coupling recorded in Pleistocene sediments off Prydz Bay (East Antarctica). Palaeogeogr. Palaeoclimatol. Palaeoecol. 485, 260–270. https://doi.org/10.1016/j.palaeo.2017.06.018.
- Wu, L., Wilson, D.J., Wang, R., Passchier, S., Krijgsman, W., Yu, X., Wen, T., Xiao, W., Liu, Z., 2021. Late quaternary dynamics of the lambert glacier-amery ice shelf system, east Antarctica. Quat. Sci. Rev. 252, 106738 https://doi.org/10.1016/j. quascirev.2020.106738.